Pulse Shape-Aided Multipath Parameter Estimation for Fine-Grained WiFi Sensing

Ke Xu, Rui Zhang, and He Chen, *Member, IEEE*

***Abstract*— Due to the finite bandwidth of practical wireless systems, one multipath component can manifest itself as a discrete pulse consisting of multiple taps in the digital delay domain. This effect is called *channel leakage*, which complicates the multipath parameter estimation. In this study, we propose a new algorithm to estimate multipath parameters, including delay, angle of arrival (AOA), and angle of departure (AOD) of leaked channels. This is accomplished by leveraging the knowledge of pulse shaping functions, a technique that can be applied to enhance the precision of WiFi sensing. More specifically, we formulate the channel impulse response (CIR) between a transmit and a receive antenna as a linear combination of a set of overcomplete basis vectors, each corresponding to a different delay. Considering the limited number of paths in physical environments, we formulate the multipath parameter estimation as a group sparse recovery problem. We develop a two-stage approach based on variational expectation maximization (VEM) to solve the formulated problem. In the first stage, we estimate the sparse vectors and determine the number of physical paths and their associated delay parameters from the positions of the nonzero entries. In the second stage, we use Newton's method to estimate the AOA and AOD of each path. The Cramér-Rao lower bound (CRLB) for multipath parameter estimation is derived for performance evaluation. Simulation results show that our algorithm can achieve superior estimation accuracy in multipath parameters compared to two benchmarking schemes and approach the CRLB.**

***Index Terms*— Channel leakage, multipath parameter estimation, pulse shaping, variational expectation maximization, WiFi sensing.**

I. INTRODUCTION

IN THE past years, WiFi has evolved beyond its initial role of providing connectivity among wireless devices to also encompass the capability of sensing surrounding environments [2], [3], [4]. This new trend has facilitated various applications such as indoor localization [5], [6], human gesture recognition [7], [8], and vital sign detection [9], [10], making WiFi a key enabling technology in the era of the Internet of things. In current WiFi systems, orthogonal frequency division multiplexing (OFDM) is used to combat frequency-selective fading [11]. The data symbols are transmitted in parallel on multiple orthogonal subcarriers. Each symbol experiences flat fading on its subcarrier, and the fading coefficient is the channel frequency response (CFR). In the sensing area, the CFR is often referred to as channel state information (CSI). Recently, several tools have been developed to extract the CSI from commodity WiFi devices [12], [13], [14]. These complex-valued CSI can provide fine-grained information of the environment and has been widely used in WiFi sensing.

In the field of indoor localization, the path delay is a key parameter to determine the position of a target because it can reflect the distance between the target and a WiFi device. Ideally, the target position can be uniquely determined in a polar coordinate system by the delay and angle of arrival (AOA) of the direct path with respect to the WiFi device. However, it is nontrivial to obtain an accurate estimate of the path delays from CSI. In wireless systems, pulse shaping and matched filtering are performed at the transmitter and the receiver, respectively. Due to the limited system bandwidth, when the delay of a physical path is a non-integer multiple of the sampling period, the multipath component in the discrete delay domain will manifest itself as a pulse consisting of multiple taps, instead of a single tap. This effect, inherent in digital wireless systems, is called *channel leakage* [15], [16], [17], [18]. An example of the channel impulse response (CIR) with the leakage effect is illustrated in Fig. 1, in which the system has a sampling period of $T = 50\,\mathrm{ns}$ while a path arrives at $\tau = 20\,\mathrm{ns}$. Consequently, a pulse consisting of 16 taps is produced.[1]

Based on the above observation, a significant problem arises if two taps within the same pulse are recognized as two physical paths with distinct delays. This situation can lead to severe degradation of the localization accuracy, especially in multipath-assisted applications such as [19] and [20]. Although existing subspace-based methods [21], [22], [23] can directly estimate the delay parameters from the frequency domain and circumvent the above issue, these algorithms rely on the underlying assumption of using an ideal pulse shaping filter with a

Manuscript received 13 November 2023; revised 9 March 2024; accepted 28 April 2024. Date of publication 6 May 2024; date of current version 18 October 2024. This work was supported in part by the Shun Hing Institute of Advanced Engineering, The Chinese University of Hong Kong, under Project MMT 79/22; and in part by a research donation by Huawei. An earlier version of this paper was presented in part at the 2023 IEEE 24th International Workshop on Signal Processing Advances in Wireless Communications (SPAWC 2023) [DOI: 10.1109/SPAWC53906.2023.10304498]. The associate editor coordinating the review of this article and approving it for publication was S. Sugiura. *(Corresponding author: He Chen.)*

Ke Xu is with the Department of Information Engineering, The Chinese University of Hong Kong, Hong Kong SAR, China (e-mail: xk020@ie.cuhk.edu.hk).

Rui Zhang and He Chen are with the Department of Information Engineering and the Shun Hing Institute of Advanced Engineering, The Chinese University of Hong Kong, Hong Kong SAR, China (e-mail: ruizhang@ie.cuhk.edu.hk; he.chen@ie.cuhk.edu.hk).

Color versions of one or more figures in this article are available at https://doi.org/10.1109/TCOMM.2024.3397838.

Digital Object Identifier 10.1109/TCOMM.2024.3397838

[1]It can be observed that around half of the taps are shifted to the end of the CIR. We will provide a detailed explanation of this phenomenon in Section II-A.

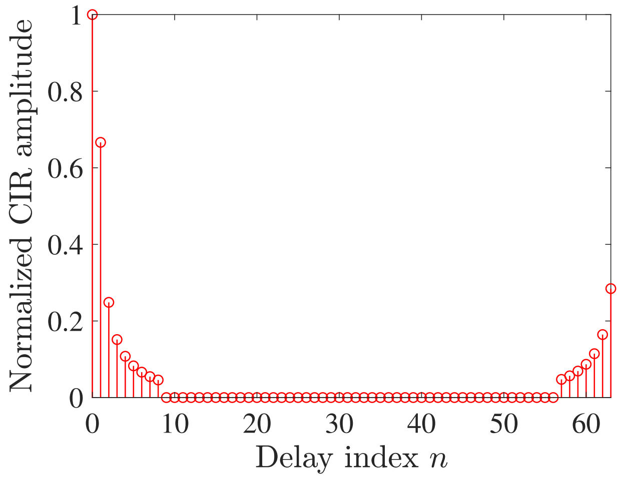

Fig. 1. Illustration of the channel leakage effect with a path delay of 20 ns and a sampling period of 50 ns. A truncated raised-cosine filter with a roll-off factor of 0.05 and a length of 16 is used.

flat frequency response on data subcarriers. However, practical pulse shaping functions have a finite time duration, incurring ripples in the passband and thus breaking the fundamental assumption of those subspace-based methods. In [24], the authors developed an atomic norm-based approach to estimate the channel and further obtain the multipath parameters by incorporating the effect of pulse shaping. However, their algorithm focuses on single-carrier systems and also imposes stringent requirements on the pulse parameters, largely limiting their practical applications.

In this study, we leverage the knowledge of the pulse shape and devise a new algorithm to estimate multipath parameters from the CSI that can be extracted from commodity WiFi devices. Since we are examining a multiple-input multiple-output (MIMO) WiFi system, it is necessary to estimate the AOA and AOD of each path, in addition to the delay parameter. Recognizing that the CIR can be seen as a superposition of multiple pulses shifted by different delays, we discretize the delay parameter into a set of grid points and formulate a group sparse recovery problem using overcomplete basis vectors composed of digital pulses that are shifted by the delays in the grid. To estimate the multipath parameters, we employ a two-stage variational expectation maximization (VEM) method. The main contributions can be summarized as follows:

- We formulate a group sparse recovery problem by expressing the CIRs of all transmit–receive antenna pairs as linear combinations of pulse shaping functions shifted by the delay grid points, in which the sparse vectors exhibit the same sparsity pattern (i.e., the same positions of nonzero entries). With this formulation, the delay parameters and the number of paths can be readily identified from the nonzero positions of the sparse vectors.
- We propose a two-stage VEM-based algorithm to solve the group sparse recovery problem. In the first stage, we assign a common Gaussian prior distribution to the path amplitudes of a grid point of all transmit–receive antenna pairs, in which the sparsity pattern is controlled by the variance parameter. The posterior distribution of the path amplitudes is obtained iteratively. Upon convergence, the delay parameters can be determined from the sparsity pattern. In the second stage, we fix the number of paths obtained from the previous stage and further estimate the AOA and AOD from the path amplitudes via Newton's method within the VEM framework. For performance evaluation, we derive the Cramér-Rao lower bound (CRLB) for the estimator, which incorporates the effect of pulse shaping.
- We finally evaluate the performance of the proposed algorithm through simulations and compare it with two existing schemes. Simulation results show that the proposed scheme achieves superior performance in multipath parameter estimation and can asymptotically approach the CRLB.

It is worth noting that the effect of pulse shaping and the problem of high-resolution delay estimation have been extensively investigated in the existing literature. In [15], [16], [17], and [18], the authors studied the pulse shaping effect and estimated the channel matrices as a whole, instead of focusing on specific multipath parameters. By leveraging the knowledge of the pulse shape, orthogonal matching pursuit (OMP)-based methods have been proposed in [25], [26] and [27], [28] for single-antenna and multi-antenna systems, respectively. Nevertheless, as shown in our previous work [1], the OMP-based method achieves inferior performance due to its greedy nature, even when the number of paths is given. In [29], [30], [31], and [32], super-resolution delay estimation algorithms based on pulse shape knowledge have been developed to overcome the low-precision limitation due to the restricted sampling rate. However, these algorithms are limited to single-antenna systems and do not incorporate the estimation of AOA and AOD. While joint delay and AOA estimation has been studied in [33], [34], and [35], the pulse shaping effect is not considered in these works. In [36], the authors subtly incorporated the knowledge of the pulse shape and introduced a space-alternating generalized expectation maximization (SAGE) algorithm to estimate the parameters of each path. In [37], a sparse variational Bayesian (VB) extension of SAGE was proposed. However, in the context of WiFi sensing, such as indoor environments, the multipath delay parameters tend to be closely spaced. As a result, these algorithms cannot distinguish each individual path from the highly overlapped pulses in the delay domain, especially when dealing with a relatively large number of paths. This issue results in a significant degradation in the estimation performance. We will further elaborate on the limitations of the two approaches in the simulation section of this paper.

The rest of the paper is organized as follows. In Section II, we introduce the MIMO WiFi channel model that incorporates the effect of pulse shaping and then formulate the group sparse recovery problem. In Section III, we elaborate on the two-stage VEM-based algorithm to estimate the channel parameters. In Section IV, simulations are conducted to validate the effectiveness of the proposed algorithm. Finally, we conclude the paper in Section V.

Notations: Boldface uppercase and lowercase letters represent matrices and column vectors, respectively. The (m, n)-th entry of matrix $\mathbf{A}$ is denoted by $A_{m,n}$, and the n-th entry of vector $\mathbf{a}$ is denoted by a_n. $\mathbb{R}$ ($\mathbb{C}$), $\mathbb{R}^N$ ($\mathbb{C}^N$), and $\mathbb{R}^{M\times N}$ ($\mathbb{C}^{M\times N}$) denote the set of real (complex)-valued scalars, vectors of size N, and matrices of size $M \times N$, respectively. For a matrix $\mathbf{A}$, the notations $\mathbf{A}^T$, $\mathbf{A}^*$, $\mathbf{A}^H$, and $\mathbf{A}^{-1}$ denote its transpose, conjugate, conjugate transpose, and inverse, respectively. $\mathrm{tr}(\cdot)$ denotes the trace of a square matrix. $|\cdot|$ denotes the magnitude of a complex number, the determinant of a matrix, or the cardinality of a set. $\mathrm{diag}(\mathbf{a})$ is a diagonal matrix with the entries in $\mathbf{a}$ on the diagonal, and $\mathrm{Diag}(\mathbf{A})$ is a diagonal matrix with the diagonal entries in $\mathbf{A}$ on the diagonal. $\mathbf{I}_N$ is an identity matrix of size $N \times N$. $\odot$ is the Hadamard product of two matrices. For two real symmetric matrices $\mathbf{A}$ and $\mathbf{B}$, $\mathbf{A} \succeq \mathbf{B}$ indicates that $\mathbf{A} - \mathbf{B}$ is positive semidefinite. $\|\cdot\|_2$ is the Euclidean norm of a vector. $p(\mathbf{x}; a)$ is the probability density function of $\mathbf{x}$ with parameter a, and $p(\mathbf{x}|\mathbf{y})$ is the probability density function of $\mathbf{x}$ conditioned on $\mathbf{y}$. $\exp(\cdot)$ is the exponential function with base e. $\ln(\cdot)$ and $\log_2(\cdot)$ are the natural logarithm function and the binary logarithm function, respectively. $\delta(\cdot)$ is the Dirac delta function. $\Gamma(\cdot)$ is the Gamma function. $\otimes$ denotes the convolution operation. $\mathcal{CN}(\mathbf{x}; \boldsymbol{\mu}, \boldsymbol{\Sigma}) = \pi^{-N}|\boldsymbol{\Sigma}|^{-1}\exp\left(-(\mathbf{x}-\boldsymbol{\mu})^H\boldsymbol{\Sigma}^{-1}(\mathbf{x}-\boldsymbol{\mu})\right)$ represents the probability density function of a complex Gaussian-distributed random vector $\mathbf{x}$ of length N, with mean $\boldsymbol{\mu}$ and covariance matrix $\boldsymbol{\Sigma}$. $\mathrm{Gamma}(x; a, b) = b^a x^{a-1}\exp(-bx)/\Gamma(a)$ represents the probability density function of a Gamma-distributed random variable with shape parameter a and rate parameter b. $\mathbb{E}[\,\cdot\,]_{p(\cdot)}$ denotes the expectation with respect to distribution $p(\cdot)$. $\mathrm{Re}\{\cdot\}$ and $\mathrm{Im}\{\cdot\}$ represent the real and imaginary parts of the argument, respectively. For a scalar $y \in \mathbb{R}$ and a vector $\mathbf{x} \in \mathbb{R}^N$, where y is a function of $\mathbf{x}$, $\partial y/\partial \mathbf{x} \in \mathbb{R}^N$ is a vector with the n-th entry given by $\partial y/\partial x_n$. For a scalar $z \in \mathbb{R}$ and two vectors $\mathbf{x} \in \mathbb{R}^M$ and $\mathbf{y} \in \mathbb{R}^N$, where z is a function of $\mathbf{x}$ and $\mathbf{y}$, $\partial^2 z/\partial\mathbf{x}\partial\mathbf{y}^T \in \mathbb{R}^{M\times N}$ is a matrix with the (m, n)-th entry given by $\partial^2 z/\partial x_m \partial y_n$. For two vectors $\mathbf{x} \in \mathbb{R}^M$ and $\mathbf{y} \in \mathbb{R}^N$, where $\mathbf{y}$ is a function of $\mathbf{x}$, $\partial\mathbf{y}/\partial\mathbf{x}^T \in \mathbb{R}^{N\times M}$ is a matrix with the (n, m)-th entry given by $\partial y_n/\partial x_m$.

II. Channel Model and Problem Formulation

In this section, we first introduce the WiFi channel model which takes into account the effect of pulse shaping, and explain how the channel delay parameters are typically used in WiFi sensing. Then, we leverage the knowledge of the pulse shape to formulate multipath parameter estimation as a group sparse recovery problem.

A. Channel Model

We consider a WiFi system with M transmit antennas and N receive antennas. The physical multipath channel between the m-th transmit antenna and the n-th receive antenna in the delay domain can be expressed as

$$h^{\mathrm{p}}_{m,n}(\tau) = \sum_{\ell=1}^{L} \alpha_{m,n,\ell}\,\delta(\tau - \tau_\ell), \tag{1}$$

where $m \in \{1, \cdots, M\}$, $n \in \{1, \cdots, N\}$, L is the number of paths, and $\alpha_{m,n,\ell}$ and τ_ℓ are the complex amplitude and the delay of the ℓ-th path, respectively. In the above equation, we assume that the delay parameters of a physical path are the same for all transmit–receive antenna pairs because the antenna spacing on a WiFi device is much smaller than the propagation distance of the signal and thus can be ignored. In addition, $\alpha_{m,n,\ell}$ can be further written as

$$\alpha_{m,n,\ell} = \alpha_{1,1,\ell}\exp\left(-\frac{j2\pi(n-1)d\sin\theta_\ell}{\lambda}\right) \times \exp\left(-\frac{j2\pi(m-1)d\sin\varphi_\ell}{\lambda}\right), \tag{2}$$

where θ_ℓ and φ_ℓ are the AOA and AOD of the ℓ-th path, d is the spacing between two adjacent antennas, and λ is the wavelength of the signal. A composite channel incorporating the effect of pulse shaping is given by

$$\begin{aligned} h_{m,n}(\tau) &= h^{\mathrm{p}}_{m,n}(\tau) \otimes g_{\mathrm{t}}(\tau) \otimes g_{\mathrm{r}}(\tau) = h^{\mathrm{p}}_{m,n}(\tau) \otimes g(\tau) \\ &= \sum_{\ell=1}^{L} \alpha_{m,n,\ell}\, g(\tau - \tau_\ell), \end{aligned} \tag{3}$$

where $g_{\mathrm{t}}(\tau)$ and $g_{\mathrm{r}}(\tau)$ are the pulse shaping filter at the transmitter and the matched filter at the receiver, respectively, and $g(\tau) \triangleq g_{\mathrm{t}}(\tau) \otimes g_{\mathrm{r}}(\tau)$. In this paper, we consider a truncated raised-cosine pulse function,[2] i.e.,

$$g(\tau) = \mathrm{sinc}\left(\frac{\tau}{T}\right)\frac{\cos\left(\frac{\pi\rho\tau}{T}\right)}{1-\left(\frac{2\rho\tau}{T}\right)^2}\, w\left(\frac{\tau}{L_{\mathrm{p}}T}\right), \tag{4}$$

where T is the sampling period, ρ is the roll-off factor, $\mathrm{sinc}(\tau) = \sin(\pi\tau)/(\pi\tau)$ is the sinc function, and $w(\tau)$ is a window function such that $w(\tau) = 1$ for $|\tau| \le 1$ and $w(\tau) = 0$ otherwise. Hence, $2L_{\mathrm{p}}T$ is the nonzero duration of the pulse function with L_{p} denoting the number of taps in half of a digital pulse. Discretizing the composite channel in (3), we have

$$h_{m,n,r} = h_{m,n}(rT) = \sum_{\ell=1}^{L} \alpha_{m,n,\ell}\, g(rT - \tau_\ell), \tag{5}$$

where $r \in \{1, \cdots, R\}$ is the delay index, and R corresponds to the maximum delay spread of the composite channel. The leakage effect is evident from (5): a physical path produces a single tap in the digital delay domain only when the path delay is an integer multiple of the sampling period; otherwise, the energy of the path will leak to multiple taps in a pulse, making it nontrivial to figure out the exact delay.

For a WiFi OFDM system with K subcarriers, the frequency response of the composite channel on subcarrier k is given by

$$\tilde{h}_{m,n,k} = \sum_{r=1}^{R} h_{m,n,r}\exp\left(-\frac{j2\pi(k-1)(r-1)}{K}\right), \tag{6}$$

where $k \in \{1, \cdots, K\}$. In practical WiFi systems, only a subset of subcarriers are used to transmit data/pilot symbols. For example, in IEEE 802.11a, the 1-st subcarrier is left unused

[2] We remark that the proposed multipath estimation framework also applies to other pulse functions.

due to the strong DC interference, and subcarriers indexed from 28 to 38 are also excluded to avoid interference from neighboring channels. In this paper, we will estimate multipath parameters from the CSI on those subcarriers available for data/pilot transmission.

It is important to note that the form of the CIR given in (5), which contains the absolute delay parameters of the physical paths, is not practically available by performing inverse Fourier transform on the measured CSI in WiFi systems. Instead, only relative delay information can be obtained from the CSI. Let us use a simple signal model to explain the reason in the following. Denote by $\mathbf{s} = [s_1, \cdots, s_{N_s}]^T$ the preamble in a WiFi packet used to estimate the CSI, which has a good autocorrelation property, i.e.,

$$\sum_n s_n s_{n-m}^* = \begin{cases} 1, & \text{if } m = 0, \\ 0, & \text{otherwise.} \end{cases} \tag{7}$$

We assume that there is only one physical path in the channel, and the path delay τ is not an integer multiple of the sampling period T. As a consequence, multiple taps are produced in the delay domain. We denote the composite CIR by $\mathbf{h} = [h_1, \cdots, h_{N_h}]^T$. Ignoring the additive noise, the received signal can be written as

$$y_n = \sum_k s_{n-k} h_k. \tag{8}$$

At the receiver, packet detection is performed by cross-correlating the received signal with the preamble:

$$\begin{aligned} r_m &= \sum_n y_n s_{n-m}^* = \sum_n \sum_k s_{n-k} h_k s_{n-m}^* \\ &= \begin{cases} h_k, & \text{if } m = k, \\ 0, & \text{otherwise,} \end{cases} \end{aligned} \tag{9}$$

which actually indicates that $r_m = h_m$. Then, the transmitted signal is considered to arrive at the receiver at $m_0 = \arg\max_m |r_m| = \arg\max_m |h_m|$, corresponding to the tap with the largest CIR amplitude. In WiFi systems, only the received signals after this time instant m_0 are used for CSI estimation. Consequently, the delay estimated from the CSI is $\hat{\tau} = \tau - m_0 T$, implying that the absolute delay information is lost, and one can only recover the relative delay of the paths from the CSI. This issue is also reflected in Fig. 1, where the tap with the largest amplitude is located at the origin, and the taps preceding this point are shifted to the end of the CIR due to the use of cyclic prefix (CP) in WiFi OFDM. Similar illustrations can also be found in [38]. To address the above problem, one may consider using time stamps that record the start time of transmission to calculate the absolute delay. However, the reliability of this method is often hindered by the lack of perfect synchronization between the transmitter and the receiver [5], [20]. Moreover, the packet detection process introduces an additional delay, which is even larger than the propagation delay of the signal, making it challenging to determine the exact time when the signal arrives [39]. For the above reasons, relative delay and angle-based approaches are preferred in WiFi sensing systems. Hereafter, for the formulation of the delay estimation problem, we do not account for the delay shift shown in Fig. 1, because we can always shift the taps at the end of the CIR back to the beginning.

B. Problem Formulation

Denote $\mathbf{h}_{m,n} = [h_{m,n,1}, \cdots, h_{m,n,R}]^T$ and $\tilde{\mathbf{h}}_{m,n} = [\tilde{h}_{m,n,1}, \cdots, \tilde{h}_{m,n,K}]^T$. The relationship between $\mathbf{h}_{m,n}$ and $\tilde{\mathbf{h}}_{m,n}$ can be written as

$$\tilde{\mathbf{h}}_{m,n} = \mathbf{F}_{1:R} \mathbf{h}_{m,n}, \tag{10}$$

where $\mathbf{F}_{1:R} \in \mathbb{C}^{K \times R}$ is a partial discrete Fourier transform (DFT) matrix composed of the first R columns of a complete DFT matrix $\mathbf{F} \in \mathbb{C}^{K \times K}$, with the (i,j)-th entry of $\mathbf{F}$ given by $F_{i,j} = \exp(-j2\pi(i-1)(j-1)/K)$. As mentioned in Section II, only a portion of the frequency response is available. Therefore, the measured CSI can be written as

$$\mathbf{y}_{m,n} = \mathbf{F}_{\mathcal{K},1:R} \mathbf{h}_{m,n} + \mathbf{n}_{m,n}, \tag{11}$$

where $\mathbf{y}_{m,n} \in \mathbb{C}^{|\mathcal{K}|}$ is the measured CSI, $\mathcal{K}$ is the index set of subcarriers used for data/pilot transmission, $\mathbf{F}_{\mathcal{K},1:R} \in \mathbb{C}^{|\mathcal{K}| \times R}$ is a matrix composed of $|\mathcal{K}|$ rows of $\mathbf{F}_{1:R}$ corresponding to the used subcarriers, and $\mathbf{n}_{m,n} \in \mathbb{C}^{|\mathcal{K}|}$ is the complex Gaussian-distributed measurement error with zero mean and variance σ^2.

Taking into account the knowledge of the pulse shape, $\mathbf{h}_{m,n}$ can be further written as

$$\mathbf{h}_{m,n} = \mathbf{A} \boldsymbol{\alpha}_{m,n}, \tag{12}$$

where $\mathbf{A} \in \mathbb{R}^{R \times L}$ and its (r,ℓ)-th entry is given by $A_{r,\ell} = g(rT - \tau_\ell)$, and $\boldsymbol{\alpha}_{m,n} = [\alpha_{m,n,1}, \cdots, \alpha_{m,n,L}]^T$. Motivated by the expression in (12), we can discretize the delay parameter into a set of fine-grained grid points as $\{pT_\text{g}\}_{p=1}^P$, where T_g is the resolution of the grid, P is the number of grid points, and PT_g is the maximum potential delay spread of the physical paths. Then, we can construct a dictionary matrix $\mathbf{A}' \in \mathbb{R}^{R \times P}$ with its (r,p)-th entry given by $A'_{r,p} = g(rT - pT_\text{g})$, and (12) can be approximated as

$$\mathbf{h}_{m,n} \approx \mathbf{A}' \boldsymbol{\alpha}'_{m,n}, \tag{13}$$

where $\boldsymbol{\alpha}'_{m,n} = [\alpha'_{m,n,1}, \cdots, \alpha'_{m,n,P}]^T$ consists of the amplitudes of the potential paths with the delays in the grid. In (13), when the delay of a path falls on a specific grid point, the corresponding entry in $\boldsymbol{\alpha}'_{m,n}$ will be nonzero. Due to the limited number of paths in the physical environment, there are only a small fraction of nonzero entries in $\boldsymbol{\alpha}'_{m,n}$. In other words, $\boldsymbol{\alpha}'_{m,n}$ is sparse. In addition, since the channels of all transmit–receive antenna pairs share the same delay parameters, the sparse vectors $\{\boldsymbol{\alpha}'_{m,n}\}_{m=1,n=1}^{M,N}$ have the same sparsity pattern (i.e., the same positions of nonzero entries). Substituting (13) into (11), we have

$$\mathbf{y}_{m,n} \approx \mathbf{F}_{\mathcal{K},1:R} \mathbf{A}' \boldsymbol{\alpha}'_{m,n} + \mathbf{n}_{m,n} = \mathbf{B} \boldsymbol{\alpha}'_{m,n} + \mathbf{n}_{m,n}, \tag{14}$$

where $\mathbf{B} \triangleq \mathbf{F}_{\mathcal{K},1:R} \mathbf{A}' \in \mathbb{C}^{|\mathcal{K}| \times P}$. Next, our objective is to recover $\boldsymbol{\alpha}'_{m,n}$ from $\mathbf{y}_{m,n}$ given $\mathbf{B}$ for all m and n, and determine the delay parameters from the positions of their nonzero entries. After the delay parameters are obtained, we can further estimate the AOA and AOD parameters from the path amplitudes.

III. VEM-Based Two-Stage Multipath Parameter Estimation

In this section, we first provide a brief overview of the VEM methodology, and then propose a two-stage VEM-based algorithm to estimate the multipath parameters.

A. An Overview of VEM

VEM is an iterative algorithm to approximate the maximum likelihood estimation [40]. By imposing statistical properties on the sparse signals, the common sparsity pattern shared by all transmit–receive antenna pairs can be readily exploited. Furthermore, the VEM algorithm offers a systematic framework for estimating both random and nonrandom parameters in a probabilistic model, making it particularly suitable for our multipath parameter estimation problem.

The VEM involves three types of quantities: the observation $\mathbf{y}$, the hidden variable $\mathbf{z}$, and the unknown parameter $\mathbf{t}$. $\mathbf{z}$ is treated as a random variable, for which a posterior distribution is derived based on its prior distribution and the likelihood function. On the other hand, $\mathbf{t}$ is considered deterministic, and only a point estimate is obtained using the rule of maximum likelihood. According to Bayes' theorem, the posterior distribution of $\mathbf{z}$ can be written as

$$p(\mathbf{z}|\mathbf{y};\mathbf{t}) = \frac{p(\mathbf{z};\mathbf{t})p(\mathbf{y}|\mathbf{z};\mathbf{t})}{p(\mathbf{y};\mathbf{t})}, \tag{15}$$

where

$$p(\mathbf{y};\mathbf{t}) = \int p(\mathbf{z};\mathbf{t})p(\mathbf{y}|\mathbf{z};\mathbf{t})\mathrm{d}\mathbf{z} \tag{16}$$

is the marginal likelihood function that should be maximized to estimate $\mathbf{t}$. In practice, it is often difficult to directly compute the integral in $p(\mathbf{y};\mathbf{t})$. Alternatively, the VEM derives a tractable approximation of $p(\mathbf{z}|\mathbf{y};\mathbf{t})$, denoted by $q(\mathbf{z})$, based on the following principle. Noting that the logarithm of $p(\mathbf{y};\mathbf{t})$ can be written as the summation of two terms:

$$\ln p(\mathbf{y};\mathbf{t}) = \mathrm{KL}(q||p) + F(q,\mathbf{t}), \tag{17}$$

where $\mathrm{KL}(q||p)$ is the Kullback–Leibler (KL) divergence between $q(\mathbf{z})$ and $p(\mathbf{z}|\mathbf{y};\mathbf{t})$:

$$\mathrm{KL}(q||p) = -\int q(\mathbf{z}) \ln\left(\frac{p(\mathbf{z}|\mathbf{y};\mathbf{t})}{q(\mathbf{z})}\right)\mathrm{d}\mathbf{z}, \tag{18}$$

and $F(q,\mathbf{t})$ is expressed as

$$F(q,\mathbf{t}) = \int q(\mathbf{z}) \ln\left(\frac{p(\mathbf{y},\mathbf{z};\mathbf{t})}{q(\mathbf{z})}\right)\mathrm{d}\mathbf{z}. \tag{19}$$

Since $\mathrm{KL}(q||p)$ is nonnegative [41], $F(q,\mathbf{t})$ can be regarded as a lower bound of $\ln p(\mathbf{y};\mathbf{t})$. Hence, both $q(\mathbf{z})$ and $\mathbf{t}$ can be determined by maximizing this lower bound. However, when $\mathbf{z}$ consists of multiple components, e.g., $\mathbf{z} = [\mathbf{z}_1^T,\cdots,\mathbf{z}_Q^T]^T$, maximizing (19) with respect to $q(\mathbf{z})$ can be still challenging. In this case, a variational approach can be adopted, in which $q(\mathbf{z})$ is factorized as

$$q(\mathbf{z}) = \prod_{q=1}^{Q} q(\mathbf{z}_q). \tag{20}$$

In other words, the components are assumed to be mutually independent. This factorization allows computing the posterior distribution of one component at a time while keeping the others fixed.

In summary, the VEM algorithm iteratively executes a variational expectation (E)-step and a maximization (M)-step to maximize (19) with respect to $\{q(\mathbf{z}_q)\}_{q=1}^{Q}$ and $\mathbf{t}$, respectively, until convergence. The update rules for the two steps are given by

$$\ln q(\mathbf{z}_q) = \langle \ln p(\mathbf{y},\mathbf{z};\mathbf{t})\rangle_{q(\mathbf{z}_{\sim q})} + \text{const.}, \tag{21}$$

and

$$\mathbf{t} = \arg\max_{\mathbf{t}} \langle \ln p(\mathbf{y},\mathbf{z};\mathbf{t})\rangle_{q(\mathbf{z})}, \tag{22}$$

where we use $\langle\cdot\rangle_{q(\cdot)}$ to denote $\mathbb{E}[\cdot]_{q(\cdot)}$ for simplicity, $q(\mathbf{z}_{\sim q}) \triangleq \prod_{q'\neq q} q(\mathbf{z}_{q'})$, and "const." represents a constant irrelevant to $\mathbf{z}_q$. The detailed derivations of (21) and (22) can be found in [40] and are omitted in this paper. Next, we will develop a two-stage framework for the pulse shape-aided multipath parameter estimation, where the VEM is employed in both stages to estimate the delay and AOA/AOD, respectively.

B. Stage One: Delay Estimation

In this part, we establish the probabilistic model and estimate the delay parameters. To proceed, we assign a complex Gaussian prior distribution to $\{\boldsymbol{\alpha}'_{m,n}\}_{m=1,n=1}^{M,N}$:

$$p(\boldsymbol{\alpha}'|\boldsymbol{\gamma}) = \prod_{m=1}^{M}\prod_{n=1}^{N} p(\boldsymbol{\alpha}'_{m,n}|\boldsymbol{\gamma}) = \prod_{m=1}^{M}\prod_{n=1}^{N}\prod_{p=1}^{P} \mathcal{CN}(\alpha'_{m,n,p};0,\gamma_p^{-1}), \tag{23}$$

where we denote $\boldsymbol{\alpha}' = [(\boldsymbol{\alpha}'_{1,1})^T,\cdots,(\boldsymbol{\alpha}'_{M,N})^T]^T$, and $\boldsymbol{\gamma} = [\gamma_1,\cdots,\gamma_P]^T$ consists of the precision parameters (i.e., the inverse of the variance) of $\alpha'_{m,n,p}$ for all p. Since $\boldsymbol{\gamma}$ is also unknown, we adopt a Gamma hyperprior model because it is the conjugate prior for the Gaussian distribution in (23) and can facilitate the inference of the posterior distribution [42]:

$$p(\boldsymbol{\gamma}) = \prod_{p=1}^{P} p(\gamma_p) = \prod_{p=1}^{P} \mathrm{Gamma}(\gamma_p;a,b), \tag{24}$$

where we use $p(\boldsymbol{\gamma})$ and $p(\gamma_p)$ to represent $p(\boldsymbol{\gamma};a,b)$ and $p(\gamma_p;a,b)$, respectively, for simplicity. In general, the parameters a and b should take small values to make the hyperprior model non-informative. With the above prior distributions, the sparsity pattern of $\boldsymbol{\alpha}'_{m,n}$ can be reflected from the estimate of $\boldsymbol{\gamma}$. Specifically, for all m and n, when γ_p is large, $\alpha'_{m,n,p}$ is forced to be around zero; when γ_p is small, $\alpha'_{m,n,p}$ is likely to be large. Therefore, we can find the delay of a path from the position where γ_p takes a small value. We use a $\boldsymbol{\gamma}$ common to the CSI of all transmit–receive antenna pairs to exploit the fact that all the sparse vectors share the same sparsity pattern, which is referred to as *group sparsity*. It is worth mentioning that the prior model in (23) is used only to enhance the sparsity, and the actual distributions of the multipath amplitudes are not necessarily Gaussian and can be correlated through a common α_ℓ across different antennas (see (2)). We will temporarily ignore this correlation when estimating the delay parameters and reconsider it when estimating the AOA and AOD.

On the other hand, based on (14), the likelihood function for $\boldsymbol{\alpha}'$ is

$$p(\mathbf{y}|\boldsymbol{\alpha}') = \prod_{m=1}^{M}\prod_{n=1}^{N} p(\mathbf{y}_{m,n}|\boldsymbol{\alpha}'_{m,n}) = \prod_{m=1}^{M}\prod_{n=1}^{N} \mathcal{CN}\left(\mathbf{y}_{m,n}; \mathbf{B}\boldsymbol{\alpha}'_{m,n}, \beta\mathbf{I}_{|\mathcal{K}|}\right), \quad (25)$$

where $\mathbf{y} = [\mathbf{y}_{1,1}^T, \cdots, \mathbf{y}_{M,N}^T]^T$, $\beta = 1/\sigma^2$, and we denote $p(\mathbf{y}|\boldsymbol{\alpha}') \triangleq p(\mathbf{y}|\boldsymbol{\alpha}';\beta)$ and $p(\mathbf{y}_{m,n}|\boldsymbol{\alpha}'_{m,n}) \triangleq p(\mathbf{y}_{m,n}|\boldsymbol{\alpha}'_{m,n};\beta)$ for simplicity. The joint probability distribution of all the involved variables can be written as

$$p(\mathbf{y}, \boldsymbol{\alpha}', \boldsymbol{\gamma}) = p(\boldsymbol{\gamma})p(\boldsymbol{\alpha}'|\boldsymbol{\gamma})p(\mathbf{y}|\boldsymbol{\alpha}') = p(\boldsymbol{\gamma})\prod_{m=1}^{M}\prod_{n=1}^{N} p(\boldsymbol{\alpha}'_{m,n}|\boldsymbol{\gamma})p(\mathbf{y}_{m,n}|\boldsymbol{\alpha}'_{m,n}). \quad (26)$$

With the probabilistic model established, we need to estimate the posterior distributions of $\{\boldsymbol{\alpha}'_{m,n}\}_{m=1,n=1}^{M,N}$ and $\boldsymbol{\gamma}$ from (26).

Since the posterior distributions are difficult to compute directly, we use the VEM method introduced in Section III-A to approximate them. As suggested in (20), we factorize the joint posterior distribution into the following form:

$$p(\boldsymbol{\alpha}', \boldsymbol{\gamma}|\mathbf{y}) \approx q(\boldsymbol{\alpha}', \boldsymbol{\gamma}) = \left(\prod_{m=1}^{M}\prod_{n=1}^{N} q(\boldsymbol{\alpha}'_{m,n})\right)\left(\prod_{p=1}^{P} q(\gamma_p)\right). \quad (27)$$

It is worth noting that the delay estimation stage does not involve unknown deterministic parameters. Therefore, we only need to use a variational E-step to compute the posterior distributions in (27). Based on (21), the posterior distribution of each $\boldsymbol{\alpha}'_{m,n}$ can be derived as

$$\begin{aligned}
&\ln q(\boldsymbol{\alpha}'_{m,n}) \\
&= \langle \ln p(\boldsymbol{\alpha}'_{m,n}|\boldsymbol{\gamma})\rangle_{q(\boldsymbol{\gamma})} + \ln p(\mathbf{y}_{m,n}|\boldsymbol{\alpha}'_{m,n}) + \text{const.} \\
&= -\sum_{p=1}^{P}\langle\gamma_p\rangle|\alpha'_{m,n,p}|^2 - \beta\|\mathbf{y}_{m,n} - \mathbf{B}\boldsymbol{\alpha}'_{m,n}\|_2^2 + \text{const.} \\
&= -(\boldsymbol{\alpha}'_{m,n} - \boldsymbol{\mu}_{m,n})^H\boldsymbol{\Sigma}_{m,n}^{-1}(\boldsymbol{\alpha}'_{m,n} - \boldsymbol{\mu}_{m,n}) + \text{const.}, \quad (28)
\end{aligned}$$

where we omit the distribution in the subscript of $\langle\gamma_p\rangle$ for brevity, and the value of $\langle\gamma_p\rangle$ will be specified later in this section. The expressions of $\boldsymbol{\Sigma}_{m,n}$ and $\boldsymbol{\mu}_{m,n}$ are

$$\begin{aligned}
\boldsymbol{\Sigma}_{m,n} &= \left(\beta\mathbf{B}^H\mathbf{B} + \boldsymbol{\Gamma}\right)^{-1}, \\
\boldsymbol{\mu}_{m,n} &= \beta\boldsymbol{\Sigma}_{m,n}\mathbf{B}^H\mathbf{y}_{m,n}, \quad (29)
\end{aligned}$$

where $\boldsymbol{\Gamma} = \mathrm{diag}\left(\langle\boldsymbol{\gamma}\rangle\right)$ and $\langle\boldsymbol{\gamma}\rangle = [\langle\gamma_1\rangle, \cdots, \langle\gamma_P\rangle]^T$. From the last step of (28), we can identify that the posterior distribution of $\boldsymbol{\alpha}'_{m,n}$ is Gaussian with mean $\boldsymbol{\mu}_{m,n}$ and covariance matrix $\boldsymbol{\Sigma}_{m,n}$. Next, the posterior distribution of each γ_p can be derived as

$$\begin{aligned}
&\ln q(\gamma_p) \\
&= \ln p(\gamma_p) + \sum_{m=1}^{M}\sum_{n=1}^{N}\langle \ln p(\alpha'_{m,n,p}|\gamma_p)\rangle_{q(\alpha'_{m,n,p})} + \text{const.} \\
&= (a-1)\ln\gamma_p - b\gamma_p + \sum_{m=1}^{M}\sum_{n=1}^{N}\left(\ln\gamma_p - \gamma_p\langle|\alpha'_{m,n,p}|^2\rangle\right) \\
&\quad + \text{const.} \\
&= (\tilde{a}_p - 1)\ln\gamma_p - \tilde{b}_p\gamma_p + \text{const.}, \quad (30)
\end{aligned}$$

with

$$\begin{aligned}
\tilde{a}_p &= a + MN, \\
\tilde{b}_p &= b + \sum_{m=1}^{M}\sum_{n=1}^{N}\langle|\alpha'_{m,n,p}|^2\rangle, \quad (31)
\end{aligned}$$

where $\langle|\alpha'_{m,n,p}|^2\rangle = |\mu_{m,n,p}|^2 + \Sigma_{m,n,p,p}$. The last step of (30) indicates that $q(\gamma_p)$ is a Gamma distribution with the shape parameter $\tilde{a}_p$ and rate parameter $\tilde{b}_p$. The posterior expectation of γ_p is then computed as $\langle\gamma_p\rangle = \tilde{a}_p/\tilde{b}_p$.

In the delay estimation stage, we iteratively compute the posterior distributions of $\{\boldsymbol{\alpha}'_{m,n}\}_{m=1,n=1}^{M,N}$ and $\{\gamma_p\}_{p=1}^{P}$ using (28) and (30), respectively, until convergence. During the iterations, we can prune some basis vectors in the dictionary matrix whose corresponding values of $\langle\gamma_p\rangle$ are significantly large. Specifically, if $\langle\gamma_p\rangle$ is larger than a threshold, we remove the p-th column of $\mathbf{B}$ and the p-th entry of $\boldsymbol{\alpha}'_{m,n}$ for all m and n. After the algorithm converges, the posterior mean $\boldsymbol{\mu}_{m,n}$ is treated as the estimate of $\boldsymbol{\alpha}'_{m,n}$, which will be used in the AOA and AOD estimation stage, and the grid points corresponding to the remaining basis vectors are treated as the estimate of delay parameters. If the number of the remaining basis vectors exceeds a predetermined value $L_{\max}$, we select a subset of $L_{\max}$ delay estimates with the smallest values of $\langle\gamma_p\rangle$. Then, we further choose the delay estimates that are not adjacent in the delay grid points. This selection approach is driven by the observation that the columns of the dictionary matrix $\mathbf{A}'$ are highly correlated because they are constructed from the pulse shaping function shifted by closely spaced delay grid points. As a consequence, there is a high possibility that multiple delay estimates with adjacent values in the grid correspond to the same physical path. Hence, in such a scenario, we only retain the delay estimate associated with the smallest value of $\langle\gamma_p\rangle$. All the above procedures for delay estimation are summarized in Algorithm 1.

Remark 1: In Algorithm 1, the selection of η entails a tradeoff between the estimation accuracy and the computational complexity. Specifically, setting η to a smaller value increases the risk of deleting the basis vector corresponding to a true physical path, potentially compromising the estimation performance. For the choice of $L_{\max}$, since each physical path could generate multiple delay grid points with non-zero amplitudes due to the correlation between the basis vectors in $\mathbf{A}'$, the value of $L_{\max}$ should be set as several times of the typical number of physical paths in the environment. However, the delay estimation performance is robust to variations in the specific values of $L_{\max}$, which will be shown in detail in Section IV.

Remark 2: In practical WiFi systems, the design parameters of the pulse shaping function may not be publicly available

Algorithm 1 Stage One: Delay Estimation

Input: Measured CSI $\{\mathbf{y}_{m,n}\}_{m=1,n=1}^{M,N}$, hyperparameters a and b, delay grid resolution $T_{\rm g}$, threshold for deleting a basis vector η, and maximum number of paths $L_{\max}$.
Output: Delay estimates $\mathcal{T}$.
Initialization: The delay estimates $\mathcal{T} = \{T_{\rm g}, \cdots, PT_{\rm g}\} \triangleq \{\hat{\tau}_1, \cdots, \hat{\tau}_P\}$, the matrix $\mathbf{B}$, and $\langle\gamma_p\rangle = a/b$ for all p.
while *stopping criterion not met* **do**
  Compute the posterior distribution of $\{\boldsymbol{\alpha}'_{m,n}\}_{m=1,n=1}^{M,N}$ using (28).
  Compute the posterior distribution of $\{\gamma_p\}_{p=1}^{P}$ using (30).
  Delete $\{\hat{\tau}_p : \langle\gamma_p\rangle > \eta \min\{\langle\gamma_{p'}\rangle\}_{p'=1}^{|\mathcal{T}|}\}$ from $\mathcal{T}$.
  Reconstruct $\mathbf{B}$ and $\boldsymbol{\alpha}'$ using $\mathcal{T}$.
end while
if $|\mathcal{T}| > L_{\max}$ **then**
  Retain only $L_{\max}$ elements in $\mathcal{T}$ with small values of $\langle\gamma_p\rangle$.
end if
Divide $\mathcal{T}$ into multiple subsets such that the elements in each subset take adjacent values in the delay grids.
Reconstruct $\mathcal{T}$ using $\hat{\tau}_p$'s with the smallest values of $\langle\gamma_p\rangle$ in their respective subsets.

and need to be estimated. In a raised-cosine pulse shaping function, the only potentially unknown design parameter is the roll-off factor ρ. We will show in the simulations that when there is 10% error in ρ, our delay estimation algorithm achieves similar performance to the scenario without errors.

Complexity analysis of Algorithm 1: The computational complexity of Algorithm 1 primarily arises from the matrix inverse in $\boldsymbol{\Sigma}_{m,n}$, which is of order $\mathcal{O}(P^3)$ in each iteration. Noting that Algorithm 1 is closely related to sparse Bayesian learning (SBL) in [43], [44], and [45], several existing works can be applied to reduce the complexity [46], [47], [48]. More recently, a covariance-free implementation of SBL has been developed in [49]. The authors devised an unbiased estimator for the diagonal entries of the covariance matrix using a small number of probe vectors. The posterior expectation of $|\alpha'_{m,n,p}|^2$ can then be computed based on this estimator (see (31)). Moreover, the construction of probe vectors and the computation of $\boldsymbol{\mu}_{m,n}$ in (29) can be efficiently accomplished by solving a group of linear systems in parallel using the conjugate gradient (CG) method [50]. Taking into account the structure of matrix $\mathbf{B}$, the complexity of the covariance-free SBL per iteration can be decreased to $\mathcal{O}\left((L_{\rm p}P + K\log_2 K)U(D+MN)\right)$, where U is the number of CG steps and D is the number of probe vectors. While important, the reduction of computational complexity is out of the scope of this paper. As a result, we will not demonstrate fast realizations of the proposed algorithm in the simulation section.

C. Stage Two: AOA and AOD Estimation

In this part, we estimate the AOA and AOD parameters based on $\{\boldsymbol{\alpha}'_{m,n}\}_{m=1,n=1}^{M,N}$ obtained in the previous stage. Substituting (2) into (14), we have[3]

$$\mathbf{y}_{m,n} = \mathbf{B}\mathbf{D}_{m,n}\boldsymbol{\alpha}_0 + \mathbf{n}_{m,n}, \tag{32}$$

where $\boldsymbol{\alpha}_0 = [\alpha_1, \cdots, \alpha_L]^T$ with $\alpha_\ell \triangleq \alpha_{1,1,\ell}$ $(\ell = 1, \cdots, L)$, $\mathbf{D}_{m,n} = \operatorname{diag}(\mathbf{d}_{m,n}) \in \mathbb{C}^{L\times L}$, and the ℓ-th entry of $\mathbf{d}_{m,n}$ is

$$\begin{aligned} d_{m,n,\ell} = \exp&\left(-\frac{j2\pi(n-1)d\sin\theta_\ell}{\lambda}\right) \\ &\times \exp\left(-\frac{j2\pi(m-1)d\sin\varphi_\ell}{\lambda}\right). \end{aligned} \tag{33}$$

Following a form similar to (23) and (24), we assign a complex Gaussian prior to $\boldsymbol{\alpha}_0$:

$$p(\boldsymbol{\alpha}_0|\boldsymbol{\gamma}_0) = \prod_{\ell=1}^{L} \mathcal{CN}(\alpha_\ell; 0, \gamma_{0,\ell}^{-1}), \tag{34}$$

where $\boldsymbol{\gamma}_0 = [\gamma_{0,1}, \cdots, \gamma_{0,L}]^T$, and assign a Gamma prior to $\boldsymbol{\gamma}_0$:

$$p(\boldsymbol{\gamma}_0) = \prod_{\ell=1}^{L} \operatorname{Gamma}(\gamma_{0,\ell}; a, b). \tag{35}$$

Analogous to (25), the likelihood function for $\boldsymbol{\alpha}_0$ can be written as

$$\begin{aligned} p(\mathbf{y}|\boldsymbol{\alpha}_0; \boldsymbol{\theta}, \boldsymbol{\varphi}) &= \prod_{m=1}^{M}\prod_{n=1}^{N} p(\mathbf{y}_{m,n}|\boldsymbol{\alpha}_0; \boldsymbol{\theta}, \boldsymbol{\varphi}) \\ &= \prod_{m=1}^{M}\prod_{n=1}^{N} \mathcal{CN}(\mathbf{y}_{m,n}; \mathbf{B}\mathbf{D}_{m,n}\boldsymbol{\alpha}_0, \beta\mathbf{I}_{|\mathcal{K}|}), \end{aligned} \tag{36}$$

where $\boldsymbol{\theta} = [\theta_1, \cdots, \theta_L]^T$ and $\boldsymbol{\varphi} = [\varphi_1, \cdots, \varphi_L]^T$, and we include them in the distributions to indicate that they are unknown parameters to be estimated. Combining (34), (35) and (36), the joint probability distribution is expressed as

$$\begin{aligned} &p(\mathbf{y}, \boldsymbol{\alpha}_0, \boldsymbol{\gamma}_0; \boldsymbol{\theta}, \boldsymbol{\varphi}) \\ &\quad = p(\boldsymbol{\gamma}_0)p(\boldsymbol{\alpha}_0|\boldsymbol{\gamma}_0)\prod_{m=1}^{M}\prod_{n=1}^{N} p(\mathbf{y}_{m,n}|\boldsymbol{\alpha}_0; \boldsymbol{\theta}, \boldsymbol{\varphi}). \end{aligned} \tag{37}$$

In the current AOA and AOD estimation stage, we treat $\boldsymbol{\alpha}_0$ and $\boldsymbol{\gamma}_0$ as hidden variables and derive their posterior distributions in the variational E-step, and treat $\boldsymbol{\theta}$ and $\boldsymbol{\varphi}$ as unknown parameters and compute their point estimates in the M-step. In fact, $\boldsymbol{\alpha}_0$ and $\boldsymbol{\gamma}_0$ can be considered as a refined version of $\boldsymbol{\alpha}'_{m,n}$ and $\boldsymbol{\gamma}$ in the previous stage. Meanwhile, we extract the linear phase shifts in the amplitudes along the antenna array and accordingly estimate the AOA and AOD in this refining process.

[3]Note that we assume the number of paths has been determined from the delay estimation stage. As a result, there are L remaining columns in $\mathbf{B}$ and L entries in $\boldsymbol{\alpha}_0$, and α_ℓ corresponds to the amplitude of a true physical path.

Following the update rule of the variational E-step in (21), the posterior distribution of $\boldsymbol{\alpha}_0$ is derived as

$$\begin{aligned}
&\ln q(\boldsymbol{\alpha}_0)\\
&= \langle \ln p(\boldsymbol{\alpha}_0|\boldsymbol{\gamma}_0)\rangle_{q(\boldsymbol{\gamma}_0)} + \sum_{m=1}^{M}\sum_{n=1}^{N} \ln p(\mathbf{y}_{m,n}|\boldsymbol{\alpha}_0;\boldsymbol{\theta},\boldsymbol{\varphi})\\
&\quad + \text{const.}\\
&= -\sum_{\ell=1}^{L}\langle\gamma_{0,\ell}\rangle|\alpha_\ell|^2 - \sum_{m=1}^{M}\sum_{n=1}^{N}\beta\|\mathbf{y}_{m,n} - \mathbf{B}\mathbf{D}_{m,n}\boldsymbol{\alpha}_0\|_2^2\\
&\quad + \text{const.}\\
&= -(\boldsymbol{\alpha}_0 - \boldsymbol{\mu}_0)^H\boldsymbol{\Sigma}_0^{-1}(\boldsymbol{\alpha}_0 - \boldsymbol{\mu}_0) + \text{const.}, \qquad (38)
\end{aligned}$$

with

$$\begin{aligned}
\boldsymbol{\Sigma}_0 &= \left(\sum_{m=1}^{M}\sum_{n=1}^{N}\beta\mathbf{D}_{m,n}^H\mathbf{B}^H\mathbf{B}\mathbf{D}_{m,n} + \boldsymbol{\Gamma}_0\right)^{-1},\\
\boldsymbol{\mu}_0 &= \sum_{m=1}^{M}\sum_{n=1}^{N}\beta\boldsymbol{\Sigma}_0\mathbf{D}_{m,n}^H\mathbf{B}^H\mathbf{y}_{m,n}, \qquad (39)
\end{aligned}$$

where $\boldsymbol{\Gamma}_0 = \operatorname{diag}(\langle\boldsymbol{\gamma}_0\rangle)$ with $\langle\boldsymbol{\gamma}_0\rangle = [\langle\gamma_{0,1}\rangle,\cdots,\langle\gamma_{0,L}\rangle]^T$. Therefore, the posterior distribution of $\boldsymbol{\alpha}_0$ is Gaussian with mean $\boldsymbol{\mu}_0$ and covariance matrix $\boldsymbol{\Sigma}_0$. Next, the posterior distribution of $\gamma_{0,\ell}$ $(\ell = 1,\cdots,L)$ is derived as

$$\begin{aligned}
&\ln q(\gamma_{0,\ell})\\
&= \ln p(\gamma_{0,\ell}) + \langle \ln p(\alpha_\ell|\gamma_{0,\ell})\rangle_{q(\alpha_\ell)} + \text{const.}\\
&= (a-1)\ln\gamma_{0,\ell} - b\gamma_{0,\ell} + \ln\gamma_{0,\ell} - \gamma_{0,\ell}\langle|\alpha_\ell|^2\rangle + \text{const.}\\
&= (\tilde{a}_{0,\ell}-1)\ln\gamma_{0,\ell} - \tilde{b}_{0,\ell}\gamma_{0,\ell} + \text{const.}, \qquad (40)
\end{aligned}$$

with

$$\begin{aligned}
\tilde{a}_{0,\ell} &= a + 1,\\
\tilde{b}_{0,\ell} &= b + \langle|\alpha_\ell|^2\rangle, \qquad (41)
\end{aligned}$$

where $\langle|\alpha_\ell|^2\rangle = |\mu_{0,\ell}|^2 + \Sigma_{0,\ell,\ell}$. Therefore, $q(\gamma_{0,\ell})$ is the probability density function of a Gamma distribution with the shape parameter $\tilde{a}_{0,\ell}$ and rate parameter $\tilde{b}_{0,\ell}$, and the posterior expectation of $\gamma_{0,\ell}$, which is used in (39), can be computed as $\langle\gamma_{0,\ell}\rangle = \tilde{a}_{0,\ell}/\tilde{b}_{0,\ell}$.

In the M-step, we need to maximize the following objective function with respect to $\boldsymbol{\theta}$ and $\boldsymbol{\varphi}$ based on the update rule in (22):

$$\begin{aligned}
f &= \langle \ln p(\mathbf{y},\boldsymbol{\alpha}_0,\boldsymbol{\gamma}_0;\boldsymbol{\theta},\boldsymbol{\varphi})\rangle_{q(\boldsymbol{\alpha}_0)q(\boldsymbol{\gamma}_0)}\\
&= \sum_{m=1}^{M}\sum_{n=1}^{N}\left\langle -\beta\|\mathbf{y}_{m,n} - \mathbf{B}\mathbf{D}_{m,n}\boldsymbol{\alpha}_0\|_2^2\right\rangle_{q(\boldsymbol{\alpha}_0)} + \text{const.}\\
&= -\sum_{m=1}^{M}\sum_{n=1}^{N}\beta\|\mathbf{y}_{m,n} - \mathbf{B}\mathbf{D}_{m,n}\boldsymbol{\mu}_0\|_2^2\\
&\quad - \sum_{m=1}^{M}\sum_{n=1}^{N}\beta\operatorname{tr}(\mathbf{B}\mathbf{D}_{m,n}\boldsymbol{\Sigma}_0\mathbf{D}_{m,n}^H\mathbf{B}^H) + \text{const.}. \qquad (42)
\end{aligned}$$

We observe that it is difficult to obtain an analytical optimal solution to the above maximization problem, and therefore we follow [51] and employ Newton's method to maximize (42) iteratively. Since there are two parameters to be estimated, namely $\boldsymbol{\theta}$ and $\boldsymbol{\varphi}$, each time we fix one of them and perform Newton's iterations for the other. Next, we focus on the update equation of AOA in each iteration, and the AOD can be updated in a similar manner. For simplicity, we denote $\omega_\ell \triangleq (2\pi d\sin\theta_\ell)/\lambda$ and $\boldsymbol{\omega} \triangleq [\omega_1,\cdots,\omega_L]^T$. The estimate of $\boldsymbol{\omega}$ in the i-th iteration, denoted by $\boldsymbol{\omega}^{(i)}$, is updated as

$$\boldsymbol{\omega}^{(i)} = \boldsymbol{\omega}^{(i-1)} - \left(\mathbf{H}^{(i-1)}\right)^{-1}\mathbf{w}^{(i-1)}, \qquad (43)$$

where $\mathbf{H}^{(i-1)} = \partial^2 f/\partial\boldsymbol{\omega}\partial\boldsymbol{\omega}^T|_{\boldsymbol{\omega}=\boldsymbol{\omega}^{(i-1)}}$ and $\mathbf{w}^{(i-1)} = \partial f/\partial\boldsymbol{\omega}|_{\boldsymbol{\omega}=\boldsymbol{\omega}^{(i-1)}}$ are the Hessian matrix and gradient vector of f evaluated at $\boldsymbol{\omega}^{(i-1)}$, respectively. The expressions of $\partial^2 f/\partial\boldsymbol{\omega}\partial\boldsymbol{\omega}^T$ and $\partial f/\partial\boldsymbol{\omega}$ are respectively given by

$$\begin{aligned}
&\frac{\partial^2 f}{\partial\boldsymbol{\omega}\partial\boldsymbol{\omega}^T}\\
&= -\sum_{m=1}^{M}\sum_{n=1}^{N}2\beta n^2\operatorname{Re}\left\{\operatorname{diag}\left(\operatorname{diag}(\boldsymbol{\mu}_0)^H\mathbf{D}_{m,n}^H\mathbf{B}^H\mathbf{u}_{m,n}\right)\right\}\\
&\quad - \sum_{m=1}^{M}\sum_{n=1}^{N}2\beta n^2\operatorname{Re}\\
&\quad \times\left\{\operatorname{diag}(\boldsymbol{\mu}_0)^H\mathbf{D}_{m,n}^H\mathbf{B}^H\mathbf{B}\mathbf{D}_{m,n}\operatorname{diag}(\boldsymbol{\mu}_0)\right\}\\
&\quad - \sum_{m=1}^{M}\sum_{n=1}^{N}2\beta n^2\operatorname{Re}\left\{\left(\mathbf{D}_{m,n}^H\mathbf{B}^H\mathbf{B}\mathbf{D}_{m,n}\right)\odot\boldsymbol{\Sigma}_0^T\right\}\\
&\quad + \sum_{m=1}^{M}\sum_{n=1}^{N}2\beta n^2\operatorname{Re}\left\{\operatorname{Diag}\left(\mathbf{D}_{m,n}^H\mathbf{B}^H\mathbf{B}\mathbf{D}_{m,n}\boldsymbol{\Sigma}_0\right)\right\}, \quad (44)
\end{aligned}$$

and

$$\begin{aligned}
\frac{\partial f}{\partial\boldsymbol{\omega}} &= \sum_{m=1}^{M}\sum_{n=1}^{N}2\beta n\operatorname{Im}\left\{\operatorname{diag}(\boldsymbol{\mu}_0)\mathbf{D}_{m,n}\mathbf{B}^T\mathbf{u}_{m,n}^*\right\}\\
&\quad + \sum_{m=1}^{M}\sum_{n=1}^{N}2\beta n\operatorname{Im}\left\{\operatorname{Diag}\left(\mathbf{D}_{m,n}^H\mathbf{B}^H\mathbf{B}\mathbf{D}_{m,n}\boldsymbol{\Sigma}_0\right)\right\},
\end{aligned}$$

$$(45)$$

where $\mathbf{u}_{m,n} \triangleq \mathbf{y}_{m,n} - \mathbf{B}\mathbf{D}_{m,n}\boldsymbol{\mu}_0$. The derivations of (44) and (45) are presented in the Appendix.

Remark 3: In the VEM framework, it is theoretically feasible to merge the two stages and jointly estimate the delay, AOA and AOD. This can be achieved by directly incorporating the relationship of the path amplitudes across antennas in (2) at the beginning, and moving AOA and AOD estimation to the M-step of the delay estimation stage. However, this approach requires estimating numerous fake AOA and AOD parameters associated with the delay grid points that do not correspond to true physical paths, leading to substantial computational overhead and resource wastage.

Remark 4: In this paper, our primary focus is on the parameter estimation of specular multipath components, as described by the channel model in (1). However, in indoor scenarios, a large number of paths with non-resolvable parameters, known as dense multipath components (DMCs), may also exist. These components can no longer be represented using Dirac delta functions in the delay domain. In such instances, DMCs are commonly approximated as colored noise, with their statistical properties determined by the power delay profile (PDP) [52], [53], [54], [55], [56]. Consequently, an additional term representing the colored noise should be incorporated into (14) when the DMCs are considered. Nevertheless, it remains feasible to develop the multipath parameter estimation algorithm within the VEM framework. This involves modifying the likelihood functions in (25) and (36) to account for the colored noise and potentially estimating additional unknown parameters in the PDP model of the DMCs [53]. It is worth noting that the algorithms proposed in these works are mainly designed for UWB systems and certain characteristics of the PDP of the DMCs may not be directly applicable to narrowband WiFi systems.

In the AOA and AOD estimation stage, we iteratively compute the posterior distributions of $\boldsymbol{\alpha}_0$ and $\{\gamma_{0,\ell}\}_{\ell=1}^{L}$ based on (38) and (40), respectively, and the point estimates of $\boldsymbol{\theta}$ and $\boldsymbol{\varphi}$ using Newton's method. To start the iterations in Newton's method, we need a simple approach to obtain initial values of the AOA and AOD. Let us take the AOA initialization as an illustrative example, and the AOD can be initialized in a similar manner. Based on (2), the ratio of the complex amplitudes of a path on two adjacent receive antennas is

$$\frac{\alpha_{m,n,\ell}}{\alpha_{m,n-1,\ell}} = \exp\left(-\frac{j2\pi d \sin\theta_\ell}{\lambda}\right). \tag{46}$$

A coarse AOA estimate can be readily obtained from the phase of the above amplitude ratio. The estimation accuracy can be further improved by averaging over all $m \in \{1, \cdots, M\}$ and $n \in \{2, \cdots, N\}$. Moreover, a pre-iteration process is added before the AOA and AOD initialization. Specifically, we fix the number of paths and re-execute Algorithm 1 to refine the estimates of the path amplitudes such that they can be better utilized in AOA and AOD initialization. All the above steps are summarized in Algorithm 2. The computational complexity mainly arises from the matrix multiplication, which is of order $\mathcal{O}(L^2|\mathcal{K}|)$. Since the number of paths L is typically small, the complexity in the AOA and AOD estimation stage can be considered negligible compared to the delay estimation.

Algorithm 2 Stage Two: AOA and AOD Estimation

1: **Input:** Measured CSI $\{\mathbf{y}_{m,n}\}_{m=1,n=1}^{M,N}$, hyperparameters a and b, and path amplitudes $\{\alpha_{m,n,\ell}\}_{m=1,n=1,\ell=1}^{M,N,L}$ obtained in the delay estimation stage.
2: **Output:** AOA estimate $\hat{\boldsymbol{\theta}}$ and AOD estimate $\hat{\boldsymbol{\varphi}}$.
3: **Initialization:**
4: Set $\langle\gamma_{0,\ell}\rangle = a/b$ for all ℓ.
5: Carry out pre-iterations to refine $\{\alpha_{m,n,\ell}\}_{m=1,n=1,\ell=1}^{M,N,L}$.
6: Initialize $\boldsymbol{\theta}$ and $\boldsymbol{\varphi}$ using the amplitude ratio and average the results over all m and n.
7: **Iteration:**
8: **while** *stopping criterion not met* **do**
9: Compute the posterior distribution of $\boldsymbol{\alpha}_0$ using (38).
10: Compute the posterior distribution of $\{\gamma_{0,\ell}\}_{\ell=1}^{L}$ using (40).
11: Compute the AOA and AOD estimates using Newton's method.
12: **end while**

D. Derivation of CRLB

In this section, we derive the CRLB for the multipath parameter estimation incorporating the effect of pulse shaping. Since the CRLB characterizes the estimation performance of continuous-valued parameters only, we assume the number of paths is known in the derivations. Denote the collection of unknown channel parameters by $\mathbf{t} = [\boldsymbol{\alpha}_{\mathrm{R}}^T, \boldsymbol{\alpha}_{\mathrm{I}}^T, \boldsymbol{\tau}^T, \boldsymbol{\theta}^T, \boldsymbol{\varphi}^T]^T$, where $\boldsymbol{\alpha}_{\mathrm{R}} = \mathrm{Re}\{\boldsymbol{\alpha}_0\}$ and $\boldsymbol{\alpha}_{\mathrm{I}} = \mathrm{Im}\{\boldsymbol{\alpha}_0\}$ are nuisance parameters, and $\boldsymbol{\tau} = [\tau_1, \cdots, \tau_L]^T$. Let $\hat{\mathbf{t}}$ denote an unbiased estimate of $\mathbf{t}$. Then, the mean squared error (MSE) matrix satisfies the following inequality [57]:[4]

$$\mathbb{E}_{p(\mathbf{y};\mathbf{t})}\left[(\hat{\mathbf{t}}-\mathbf{t})(\hat{\mathbf{t}}-\mathbf{t})^T\right] \succeq \mathbf{J}_{\mathbf{t}}^{-1}, \tag{47}$$

where $\mathbf{J}_{\mathbf{t}}^{-1}$ is the CRLB matrix of $\mathbf{t}$, and $\mathbf{J}_{\mathbf{t}}$ is termed the Fisher information matrix (FIM). The inequality indicates that the mean squared error of each estimated parameter is lower bounded by its corresponding diagonal entry in $\mathbf{J}_{\mathbf{t}}^{-1}$. Additionally, the FIM has the following form:

$$\mathbf{J}_{\mathbf{t}} = \begin{bmatrix} \mathbf{J}_{\boldsymbol{\alpha}_{\mathrm{R}},\boldsymbol{\alpha}_{\mathrm{R}}} & \mathbf{J}_{\boldsymbol{\alpha}_{\mathrm{R}},\boldsymbol{\alpha}_{\mathrm{I}}} & \mathbf{J}_{\boldsymbol{\alpha}_{\mathrm{R}},\boldsymbol{\tau}} & \mathbf{J}_{\boldsymbol{\alpha}_{\mathrm{R}},\boldsymbol{\theta}} & \mathbf{J}_{\boldsymbol{\alpha}_{\mathrm{R}},\boldsymbol{\varphi}} \\ \mathbf{J}_{\boldsymbol{\alpha}_{\mathrm{I}},\boldsymbol{\alpha}_{\mathrm{R}}} & \mathbf{J}_{\boldsymbol{\alpha}_{\mathrm{I}},\boldsymbol{\alpha}_{\mathrm{I}}} & \mathbf{J}_{\boldsymbol{\alpha}_{\mathrm{I}},\boldsymbol{\tau}} & \mathbf{J}_{\boldsymbol{\alpha}_{\mathrm{I}},\boldsymbol{\theta}} & \mathbf{J}_{\boldsymbol{\alpha}_{\mathrm{I}},\boldsymbol{\varphi}} \\ \mathbf{J}_{\boldsymbol{\tau},\boldsymbol{\alpha}_{\mathrm{R}}} & \mathbf{J}_{\boldsymbol{\tau},\boldsymbol{\alpha}_{\mathrm{I}}} & \mathbf{J}_{\boldsymbol{\tau},\boldsymbol{\tau}} & \mathbf{J}_{\boldsymbol{\tau},\boldsymbol{\theta}} & \mathbf{J}_{\boldsymbol{\tau},\boldsymbol{\varphi}} \\ \mathbf{J}_{\boldsymbol{\theta},\boldsymbol{\alpha}_{\mathrm{R}}} & \mathbf{J}_{\boldsymbol{\theta},\boldsymbol{\alpha}_{\mathrm{I}}} & \mathbf{J}_{\boldsymbol{\theta},\boldsymbol{\tau}} & \mathbf{J}_{\boldsymbol{\theta},\boldsymbol{\theta}} & \mathbf{J}_{\boldsymbol{\theta},\boldsymbol{\varphi}} \\ \mathbf{J}_{\boldsymbol{\varphi},\boldsymbol{\alpha}_{\mathrm{R}}} & \mathbf{J}_{\boldsymbol{\varphi},\boldsymbol{\alpha}_{\mathrm{I}}} & \mathbf{J}_{\boldsymbol{\varphi},\boldsymbol{\tau}} & \mathbf{J}_{\boldsymbol{\varphi},\boldsymbol{\theta}} & \mathbf{J}_{\boldsymbol{\varphi},\boldsymbol{\varphi}} \end{bmatrix}. \tag{48}$$

For any two subvectors $\mathbf{t}_i, \mathbf{t}_j \in \{\boldsymbol{\alpha}_{\mathrm{R}}, \boldsymbol{\alpha}_{\mathrm{I}}, \boldsymbol{\tau}, \boldsymbol{\theta}, \boldsymbol{\varphi}\}$, the submatrix $\mathbf{J}_{\mathbf{t}_i,\mathbf{t}_j}$ is expressed as

$$\mathbf{J}_{\mathbf{t}_i,\mathbf{t}_j} = -\mathbb{E}_{p(\mathbf{y};\mathbf{t})}\left[\frac{\partial^2 \ln p(\mathbf{y};\mathbf{t})}{\partial \mathbf{t}_i \partial \mathbf{t}_j^T}\right]. \tag{49}$$

Using the Slepian-Bangs formula [58], $\mathbf{J}_{\mathbf{t}_i,\mathbf{t}_j}$ can be further written as

$$\begin{aligned} \mathbf{J}_{\mathbf{t}_i,\mathbf{t}_j} &= 2\beta \sum_{m=1}^{M}\sum_{n=1}^{N}\sum_{k=1}^{|\mathcal{K}|} \mathrm{Re}\left\{\frac{\partial y_{m,n,k}^*}{\partial \mathbf{t}_i}\frac{\partial y_{m,n,k}}{\partial \mathbf{t}_j^T}\right\} \\ &= 2\beta \sum_{m=1}^{M}\sum_{n=1}^{N}\sum_{k\in\mathcal{K}} \mathrm{Re}\left\{\frac{\partial \tilde{h}_{m,n,k}^*}{\partial \mathbf{t}_i}\frac{\partial \tilde{h}_{m,n,k}}{\partial \mathbf{t}_j^T}\right\}, \end{aligned} \tag{50}$$

where $\tilde{h}_{m,n,k}$ is given in (6). Notably, (50) only involves straightforward derivative calculations, and thus further details are omitted for brevity.

E. Relevant Discussions on WiFi Sensing

An accurate estimate of multipath parameters not only benefits WiFi-based sensing applications, but also suggests an efficient representation of the CSI data. In practical WiFi sensing scenarios, multiple WiFi devices are often deployed at different locations to cooperatively perform sensing tasks. In such cases, the measurement results of each WiFi device should be reported to a central unit for further processing, a

[4]We do not incorporate the prior distribution of $\boldsymbol{\alpha}_0$ and compute a Bayesian CRLB, because the prior model is only used to enhance the sparsity and facilitate the inference of the posterior distribution in the proposed algorithm, but does not reflect the true distribution of the path amplitudes. Consequently, the whole parameter vector $\mathbf{t}$ is treated deterministic, and the randomness of this probabilistic model is fully characterized by $p(\mathbf{y};\mathbf{t})$ in the subscript of the expectation in (47).

process known as *feedback* [59]. Selecting an appropriate feedback type, i.e., the data format that represents the measurement results, requires careful consideration to ensure that sufficient environmental information is preserved in the feedback data. Several feedback types for IEEE 802.11bf in the sub-7 GHz and 60 GHz bands have been detailed in [59]. Although the full CSI matrix retains all the essential sensing information, it introduces a substantial communication overhead during the feedback process. To mitigate the volume of feedback data, various alternative feedback types have also been proposed, such as the partial CSI matrix, truncated CIR matrix, and target-related parameters. Nevertheless, these feedback types still pose a significant feedback overhead when the transceivers are equipped with multiple antennas or are exclusively suited for a specific sensing application.

Given the aforementioned limitations, an ideal feedback type should be capable of reconstructing the entire CSI data to support a wide range of sensing applications while keeping a small data volume. Notably, the multipath parameters estimated from our proposed algorithm, which only include the delay, AOA, AOD, and amplitude of each path, satisfy both of these requirements and offer a promising alternative to conventional feedback approaches. Furthermore, as the CSI is reconstructed solely from these pertinent multipath parameters, the noise in the originally measured CSI can be effectively suppressed. In essence, the proposed algorithm yields a "cleaned" version of the CSI data, enhancing its overall quality and reliability.

IV. Simulations

In this section, the performance of the proposed multipath parameter estimation algorithm is evaluated through simulations. The carrier frequency of the WiFi system is $f_c = 2.4\,\mathrm{GHz}$. The system bandwidth is $f_s = 20\,\mathrm{MHz}$, corresponding to a sampling period $T = 50\,\mathrm{ns}$.[5] Out of a total number of $K = 64$ subcarriers, 52 are used for data/pilot transmission with indices from 2 to 27 and from 39 to 64. The length of the cyclic prefix is set to 32, which is the same as the length of the delay-domain composite channel R. We use a raised-cosine pulse function with the roll-off factor $\rho = 0.05$, truncated to a nonzero duration of $16T$. In other words, $L_p = 8$. Both the transmitter and the receiver are equipped with 3 antennas with the antenna spacing equal to half the wavelength. The number of paths is 3 with the parameters set as $\tau_1 = 24\,\mathrm{ns}$, $\tau_2 = 65\,\mathrm{ns}$, $\tau_3 = 95\,\mathrm{ns}$, $\theta_1 = 30°$, $\theta_2 = 45°$, $\theta_3 = 60°$, $\varphi_1 = 30°$, $\varphi_2 = 45°$, and $\varphi_3 = 60°$. Note that the delay difference between any two adjacent paths is smaller than the sampling period. The signal-to-noise ratio (SNR) is defined as the ratio between the power of the first path $|\alpha_1|^2$ to the variance of the CSI measurement error σ^2. We generate the complex path amplitudes based on the ray-tracing model described in [61]. Specifically, for $\ell \in \{2, \cdots, L\}$, the amplitude of α_ℓ is determined as $R_\ell|\alpha_1|\tau_1/\tau_\ell$, where we set $R_2 = R_3 = 1$ for simplicity, and the phase of α_ℓ is given by $-2\pi f_c \tau_\ell$. In the proposed multipath parameter estimation algorithm, the grid resolution is set to $T_g = 1\,\mathrm{ns}$. The number of grid points is $P = 100$, corresponding to a maximum delay spread of $cPT_g = 30\,\mathrm{m}$. The hyperparameters in the Gamma distribution are set as $a = b = 1 \times 10^{-6}$, and we initialize $\langle\gamma_p\rangle = a/b$ and $\langle\gamma_{0,\ell}\rangle = a/b$ in the two stages. A threshold of $\eta = 1 \times 10^5$ is chosen for deleting a basis vector in delay estimation. Upon convergence, we set $L_{\max} = 10$ for further delay selection. The number of iterations in Newton's method is chosen to be 100. For the VEM iterations in delay estimation, we terminate them when either the relative change of the estimated path amplitudes falls below 1×10^{-4} or the iteration count reaches 1000, and in AOA/AOD estimation, we additionally check the relative change of the AOA and AOD estimates.

[5]The 20 MHz WiFi channel has been used for sensing tasks in [6], [8], [10], [19], and [60]. However, our algorithm can also be applied to systems with larger bandwidths, such as $f_s = 40\,\mathrm{MHz}$ or $f_s = 80\,\mathrm{MHz}$.

TABLE I
Performance of Estimation of the Number of Paths

SNR (dB)	20	25	30	35	40
Probability	0.9960	1.0000	1.0000	1.0000	1.0000
MAE	0.0040	0.0000	0.0000	0.0000	0.0000

Two benchmarks are considered in this paper: the SAGE algorithm in [36] and its VB extension in [37]. Although the formulation of the SAGE-related algorithms accounts for the pulse shaping function, most studies that employ them for WiFi sensing do not incorporate the pulse shape knowledge [6], [19], [60]. In the following, we will provide simulation results of the two algorithms with and without pulse shape knowledge. In [37], the authors have demonstrated that the VB-SAGE has the ability to adaptively estimate the number of paths, in contrast to SAGE, which relies on a predetermined value. Specifically, in VB-SAGE, if the SNR of a path is smaller than a threshold, then the path is regarded as noise and discarded. However, the SNR threshold is a function of delay and should be determined from the PDP of the channel. This is not practical in a WiFi system in which the absolute delay information is lost. In light of this challenge, we input the ground truth of the number of paths in both SAGE and VB-SAGE. In addition, we use a stopping criterion for the two benchmarks similar to that for our algorithm by checking if either the relative change of all parameters is smaller than 1×10^{-4} or the number of iterations reaches 1000. All the results presented below are obtained by averaging over 2000 simulations. The computational complexities of SAGE and VB-SAGE are both $\mathcal{O}(ILMN|\mathcal{K}|(P_\tau + P_\theta + P_\varphi))$, where I is the number of iterations, $P_\tau = 100$, $P_\theta = 180$ and $P_\varphi = 180$ are the sizes of the sets of the candidate values for delay, AOA and AOD, respectively. Note that we use a grid search method to find the optimal values of the multipath parameter estimates in each iteration, in which the delay resolution is set to 1 ns and the AOA/AOD resolution is set to 1°. We remark that when a fast implementation is adopted for our proposed algorithm, its computational complexity is expected to be on par with that of SAGE and VB-SAGE.

In Table I, we show the probability of correct estimation and the mean absolute error (MAE) of the number of paths obtained by our proposed algorithm. It can be observed that

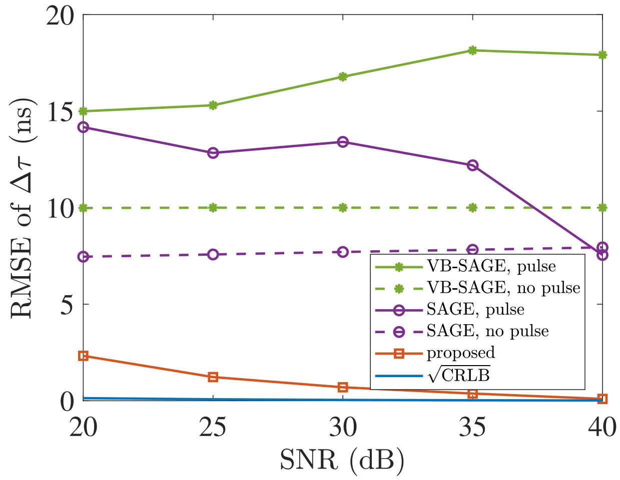

Fig. 2. Comparison of RMSE of the relative delay between the first path and the second path.

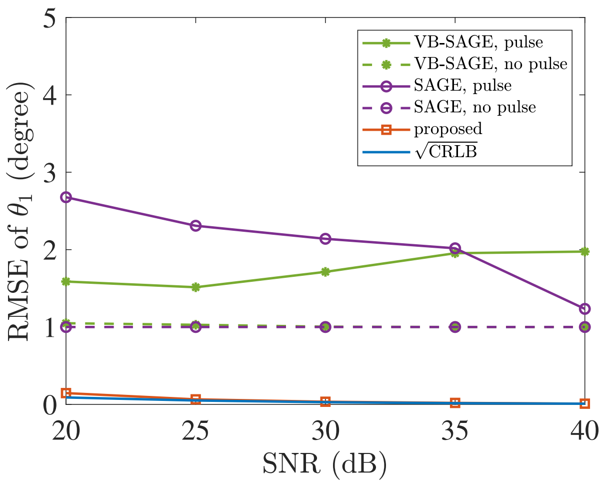

Fig. 3. Comparison of RMSE of the AOA of the first path.

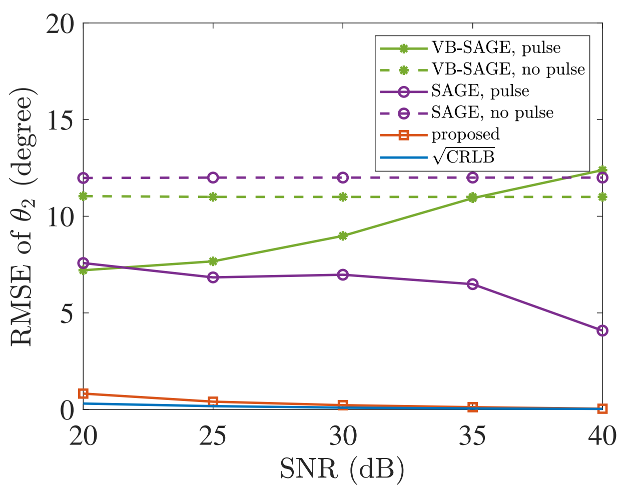

Fig. 4. Comparison of RMSE of the AOA of the second path.

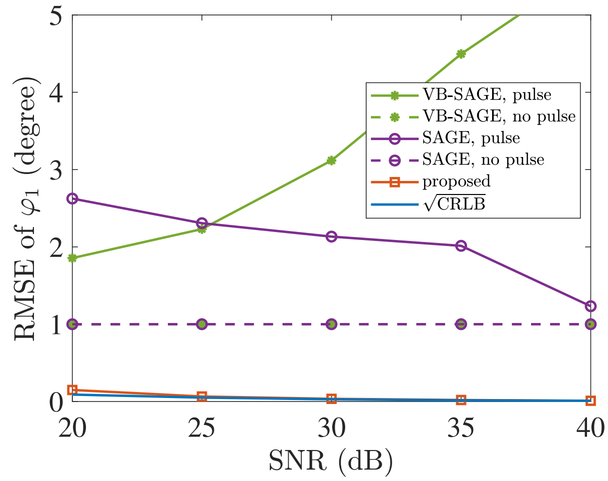

Fig. 5. Comparison of RMSE of the AOD of the first path.

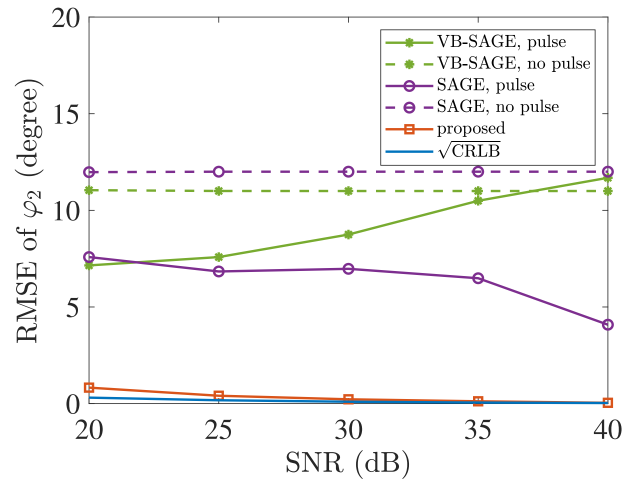

Fig. 6. Comparison of RMSE of the AOD of the second path.

our algorithm can correctly determine the number of paths. Figs. 2–6 compare the root MSE (RMSE) for the multipath parameter estimation using different algorithms, with each figure corresponding to the performance of a specific parameter. We note that we show the RMSE of the relative delay between the first and the second paths in Fig. 2 since the absolute delay information is lost after packet detection. For the AOA and AOD estimation, we plot the RMSE of the first and the second paths separately. In each trial of the proposed algorithm, RMSE is calculated only when the number of paths is larger than 1. The figures clearly demonstrate that the proposed algorithm outperforms the two benchmarks and approaches the CRLB. For SAGE and VB-SAGE, they achieve inferior performance due to the successive interference cancellation technique used in the initial stage. Specifically, the algorithm initially treats the entire CSI as a single path and estimates its delay, AOA, and AOD. Then, the estimated path is subtracted from the CSI and the estimation process continues for subsequent paths until a stopping criterion is met. However, this sequential estimation process can lead to accumulated errors, where inaccuracies in one path estimation propagate to subsequent paths. This limitation has been previously noted in [62]. This poor initialization often results in the algorithm being trapped in local optima, hindering convergence to an accurate estimate of the multipath parameters. Consequently, in [36] and [63], alternative approaches such as subspace-based methods have been suggested to mitigate

TABLE II
ESTIMATION PERFORMANCE WITH DIFFERENT VALUES OF $L_{\max}$

	$L_{\max}$	10	15	20
SNR = 20dB	RMSE	2.3264	2.3538	2.3990
	Probability	0.9960	0.9960	0.9960
	MAE	0.0040	0.0040	0.0040
SNR = 25dB	RMSE	1.2260	1.2004	1.2095
	Probability	1.0000	0.9975	0.9975
	MAE	0.0000	0.0025	0.0025
SNR = 30dB	RMSE	0.6968	0.7039	0.7011
	Probability	1.0000	1.0000	1.0000
	MAE	0.0000	0.0000	0.0000
SNR = 35dB	RMSE	0.3722	0.3748	0.3688
	Probability	1.0000	0.9995	1.0000
	MAE	0.0000	0.0005	0.0000
SNR = 40dB	RMSE	0.0949	0.0837	0.0922
	Probability	1.0000	1.0000	1.0000
	MAE	0.0000	0.0000	0.0000

TABLE III
ESTIMATION PERFORMANCE WITH DIFFERENT VALUES OF $\tilde{\rho}$

	$\tilde{\rho}$	0.045	0.05	0.055
SNR = 20dB	RMSE	2.3696	2.3264	2.4189
	Probability	0.9940	0.9960	0.9935
	MAE	0.0060	0.0040	0.0065
SNR = 25dB	RMSE	1.1952	1.2260	1.2355
	Probability	0.9990	1.0000	0.9990
	MAE	0.0010	0.0000	0.0010
SNR = 30dB	RMSE	0.7145	0.6968	0.7208
	Probability	0.9995	1.0000	1.0000
	MAE	0.0005	0.0000	0.0000
SNR = 35dB	RMSE	0.4141	0.3722	0.4284
	Probability	1.0000	1.0000	1.0000
	MAE	0.0000	0.0000	0.0000
SNR = 40dB	RMSE	0.1342	0.0949	0.1987
	Probability	1.0000	1.0000	1.0000
	MAE	0.0000	0.0000	0.0000

this initialization issue. Furthermore, we also find through the simulations that this phenomenon is more evident for delay estimation when the pulse shaping function is considered and when the multipath parameters are closely spaced. In the specific context of WiFi sensing, the pulse shapes of different paths exhibit significant overlap in the delay domain, rendering it difficult to distinguish each individual path from a superposition of multiple pulses. In addition, it can be seen that the estimation errors of VB-SAGE increase with the SNR when the pulse shaping function is considered. This behavior occurs because the poor initialization issue becomes less prominent in low-SNR conditions. In such cases, the noise acts as a perturbation, aiding the parameter estimates to "escape" from the local optima. Although the performance of SAGE/VB-SAGE is expected to improve when the subspace-based methods are used for initialization, the implementation will result in drastically increased computational complexity, especially when the steering vectors are designed in a stacked manner to jointly estimate the delay, AOA, and AOD [5], [20]. As a result, we do not employ these methods for initialization in the simulations.

In Table II, we assess the robustness of the multipath estimation algorithm to the selection of $L_{\max}$. Specifically, we show the RMSE of relative delay estimation, along with the probability of correct estimation and the MAE of the number of paths with $L_{\max} = 10$, $L_{\max} = 15$, and $L_{\max} = 20$. It can be observed that our algorithm is not sensitive to the value of $L_{\max}$. In Table III, we show the estimation performance with and without error in the roll-off factor, where the roll-off factors used in the proposed algorithm are $\tilde{\rho} = 0.045$, $\tilde{\rho} = 0.05$, and $\tilde{\rho} = 0.055$. Notably, our algorithm achieves similar performance in all three scenarios.

In Fig. 7, we compare the normalized RMSE (NRMSE) of CSI reconstruction using different algorithms, where the error is calculated in reference to the noiseless CSI instead of the measured CSI. We can observe that the NRMSE of the proposed algorithm is lower than that of SAGE and VB-SAGE. This result suggests an effective representation of CSI data using only a small number of multipath parameters, which can significantly reduce the feedback overhead in cooperative sensing scenarios.

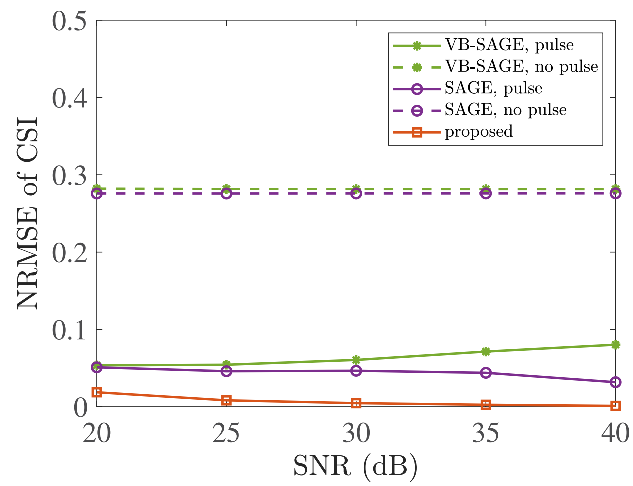

Fig. 7. Comparison of NRMSE of CSI reconstruction.

V. CONCLUSION AND FUTURE WORK

This paper presented a pulse shape-aided framework for estimating multipath parameters, including delay, AOA and AOD of each path, in MIMO WiFi channels. By accounting for the channel leakage effect (i.e., a single propagation path can manifest itself as multiple taps in the delay domain), the proposed approach can be used for fine-grained WiFi sensing. Specifically, we leveraged the knowledge of the pulse shape and formulated a group sparse recovery problem using a dictionary matrix composed of discretized pulses shifted by different delays. We proposed a two-stage method using the VEM algorithm to first estimate the multipath delays, followed by the estimation of the AOAs and AODs. Simulation results have shown that our proposed algorithm can accurately estimate the channel parameters and reconstruct the CSI data.

A limitation of this study is that in practice, pulse shaping is not always implemented via a simple raised-cosine filter, and its function is not readily available to WiFi users. In our forthcoming research, we aim to employ learning-based methods to estimate the pulse shaping function of real-world WiFi systems. Additionally, we plan to apply the multipath parameter estimation algorithm in more complex sensing scenarios.

APPENDIX
DERIVATION OF (44) AND (45)

Denote

$$f_{1,m,n} \triangleq \|\mathbf{y}_{m,n} - \mathbf{B}\mathbf{D}_{m,n}\boldsymbol{\mu}_0\|_2^2, \tag{51}$$

and

$$f_{2,m,n} \triangleq \mathrm{tr}(\mathbf{B}\mathbf{D}_{m,n}\boldsymbol{\Sigma}_0\mathbf{D}_{m,n}^H\mathbf{B}^H). \tag{52}$$

First, we compute $\partial f_{1,m,n}/\partial\boldsymbol{\omega}$ and $\partial^2 f_{1,m,n}/\partial\boldsymbol{\omega}\partial\boldsymbol{\omega}^T$. Observing that

$$\mathbf{u}_{m,n} = \mathbf{y}_{m,n} - \mathbf{B}\mathbf{D}_{m,n}\boldsymbol{\mu}_0 \triangleq \mathbf{u}_{\mathrm{R},m,n} + j\mathbf{u}_{\mathrm{I},m,n}, \tag{53}$$

where $\mathbf{u}_{\mathrm{R},m,n} = \mathrm{Re}\{\mathbf{u}_{m,n}\}$, and $\mathbf{u}_{\mathrm{I},m,n} = \mathrm{Im}\{\mathbf{u}_{m,n}\}$, we can rewrite $f_{1,m,n}$ as

$$f_{1,m,n} = \|\mathbf{u}_{m,n}\|_2^2 = \sum_{k\in\mathcal{K}} \left(u_{\mathrm{R},m,n,k}^2 + u_{\mathrm{I},m,n,k}^2\right). \tag{54}$$

Hence, for $\ell \in \{1,\cdots,L\}$,

$$\frac{\partial f_{1,m,n}}{\partial \omega_\ell} = 2\sum_{k\in\mathcal{K}}\left(u_{\mathrm{R},m,n,k}\frac{\partial u_{\mathrm{R},m,n,k}}{\partial\omega_\ell} + u_{\mathrm{I},m,n,k}\frac{\partial u_{\mathrm{I},m,n,k}}{\partial\omega_\ell}\right). \tag{55}$$

Since

$$u_{\mathrm{R},m,n,k} = \mathrm{Re}\left\{y_{m,n,k} - \sum_{\ell=1}^{L} B_{k,\ell} d_{m,n,\ell}\mu_{0,\ell}\right\}, \tag{56}$$

where $d_{m,n,\ell}$ is defined in (33), we have

$$\frac{\partial u_{\mathrm{R},m,n,k}}{\partial\omega_\ell} = -n\mathrm{Im}\left\{B_{k,\ell} d_{m,n,\ell}\mu_{0,\ell}\right\}, \tag{57}$$

In a similar fashion, we can obtain

$$\frac{\partial u_{\mathrm{I},m,n,k}}{\partial\omega_\ell} = n\mathrm{Re}\left\{B_{k,\ell} d_{m,n,\ell}\mu_{0,\ell}\right\}. \tag{58}$$

Substituting (57) and (58) into (55), we have

$$\begin{aligned}\frac{\partial f_{1,m,n}}{\partial\omega_\ell} &= -2n\mathrm{Im}\left\{\sum_{k\in\mathcal{K}} B_{k,\ell} u_{m,n,k}^* d_{m,n,\ell}\mu_{0,\ell}\right\} \\ &= -2n\mathrm{Im}\left\{\mathbf{b}_\ell^T\mathbf{u}_{m,n}^* d_{m,n,\ell}\mu_{0,\ell}\right\},\end{aligned} \tag{59}$$

where $\mathbf{b}_\ell$ is the ℓ-th column of $\mathbf{B}$. Since $(\partial f_{1,m,n}/\partial\boldsymbol{\omega})_\ell = \partial f_{1,m,n}/\partial\omega_\ell$, we obtain

$$\frac{\partial f_{1,m,n}}{\partial\boldsymbol{\omega}} = -2n\mathrm{Im}\left\{\mathrm{diag}(\boldsymbol{\mu}_0)\mathbf{D}_{m,n}\mathbf{B}^T\mathbf{u}_{m,n}^*\right\}. \tag{60}$$

Based on (55), we can compute the second-order derivative as

$$\begin{aligned}&\frac{\partial^2 f_{1,m,n}}{\partial\omega_\ell\partial\omega_{\ell'}} \\ &= 2\sum_{k\in\mathcal{K}}\left(\frac{\partial u_{\mathrm{R},m,n,k}}{\partial\omega_\ell}\frac{\partial u_{\mathrm{R},m,n,k}}{\partial\omega_{\ell'}} + \frac{\partial u_{\mathrm{I},m,n,k}}{\partial\omega_\ell}\frac{\partial u_{\mathrm{I},m,n,k}}{\partial\omega_{\ell'}}\right) \\ &+ 2\sum_{k\in\mathcal{K}}\left(u_{\mathrm{R},m,n,k}\frac{\partial^2 u_{\mathrm{R},m,n,k}}{\partial\omega_\ell\partial\omega_{\ell'}} + u_{\mathrm{I},m,n,k}\frac{\partial^2 u_{\mathrm{I},m,n,k}}{\partial\omega_\ell\partial\omega_{\ell'}}\right).\end{aligned} \tag{61}$$

When $\ell \neq \ell'$, the second summation on the right-hand side of (61) becomes zero, and then

$$\frac{\partial^2 f_{1,m,n}}{\partial\omega_\ell\partial\omega_{\ell'}} = 2n^2\mathrm{Re}\left\{(d_{m,n,\ell}\mu_{0,\ell}\mathbf{b}_\ell)^H(d_{m,n,\ell'}\mu_{0,\ell'}\mathbf{b}_{\ell'})\right\}. \tag{62}$$

When $\ell = \ell'$,

$$\frac{\partial^2 f_{1,m,n}}{\partial\omega_\ell^2} = 2n^2\|\mu_{0,\ell}\mathbf{b}_\ell\|_2^2 + 2n^2\mathrm{Re}\left\{\mathbf{b}_\ell^T\mathbf{u}_{m,n}^* d_{m,n,\ell}\mu_{0,\ell}\right\}. \tag{63}$$

Combining (62) and (63), we have

$$\begin{aligned}\frac{\partial^2 f_{1,m,n}}{\partial\boldsymbol{\omega}\partial\boldsymbol{\omega}^T} &= 2n^2\mathrm{Re}\left\{\mathrm{diag}(\boldsymbol{\mu}_0)^H\mathbf{D}_{m,n}^H\mathbf{B}^H\mathbf{B}\mathbf{D}_{m,n}\mathrm{diag}(\boldsymbol{\mu}_0)\right\} \\ &+ 2n^2\mathrm{Re}\left\{\mathrm{diag}\left(\mathrm{diag}(\boldsymbol{\mu}_0)^H\mathbf{D}_{m,n}^H\mathbf{B}^H\mathbf{u}_{m,n}\right)\right\}.\end{aligned} \tag{64}$$

Next, we compute $\partial f_{2,m,n}/\partial\boldsymbol{\omega}$ and $\partial^2 f_{2,m,n}/\partial\boldsymbol{\omega}\partial\boldsymbol{\omega}^T$. We observe that $f_{2,m,n}$ can be written as

$$f_{2,m,n} = \sum_{\ell=1}^{L}\sum_{\ell'=1}^{L}\Sigma_{0,\ell',\ell}(d_{m,n,\ell}\mathbf{b}_\ell)^H(d_{m,n,\ell'}\mathbf{b}_{\ell'}). \tag{65}$$

Therefore, we can obtain

$$\begin{aligned}\frac{\partial f_{2,m,n}}{\partial\omega_\ell} &= -2n\mathrm{Im}\left\{\sum_{\ell'=1}^{L}\Sigma_{0,\ell',\ell}(d_{m,n,\ell}\mathbf{b}_\ell)^H(d_{m,n,\ell'}\mathbf{b}_{\ell'})\right\} \\ &= -2n\mathrm{Im}\left\{(d_{m,n,\ell}\mathbf{b}_\ell)^H\mathbf{B}\mathbf{D}_{m,n}\boldsymbol{\xi}_\ell\right\},\end{aligned} \tag{66}$$

where $\boldsymbol{\xi}_\ell$ is the ℓ-th column of $\boldsymbol{\Sigma}_0$. Since $(\partial f_{2,m,n}/\partial\boldsymbol{\omega})_\ell = \partial f_{2,m,n}/\partial\omega_\ell$, we have

$$\frac{\partial f_{2,m,n}}{\partial\boldsymbol{\omega}} = -2n\mathrm{Im}\left\{\mathrm{Diag}\left(\mathbf{D}_{m,n}^H\mathbf{B}^H\mathbf{B}\mathbf{D}_{m,n}\boldsymbol{\Sigma}_0\right)\right\}. \tag{67}$$

To compute the second-order derivative $\partial^2 f_{2,m,n}/\partial\omega_\ell\partial\omega_{\ell'}$, we first consider the case when $\ell = \ell'$

$$\begin{aligned}&\frac{\partial^2 f_{2,m,n}}{\partial\omega_\ell^2} \\ &= 2n^2\Sigma_{0,\ell,\ell}\|\mathbf{b}_\ell\|_2^2 \\ &\quad - 2n^2\mathrm{Re}\left\{\sum_{\ell'=1}^{L}\Sigma_{0,\ell',\ell}(d_{m,n,\ell}\mathbf{b}_\ell)^H(d_{m,n,\ell'}\mathbf{b}_{\ell'})\right\} \\ &= 2n^2\Sigma_{0,\ell,\ell}\|\mathbf{b}_\ell\|_2^2 - 2n^2\mathrm{Re}\left\{(d_{m,n,\ell}\mathbf{b}_\ell)^H\mathbf{B}\mathbf{D}_{m,n}\boldsymbol{\xi}_\ell\right\}.\end{aligned} \tag{68}$$

Then, for $\ell \neq \ell'$, we have

$$\frac{\partial^2 f_{2,m,n}}{\partial\omega_\ell\partial\omega_{\ell'}} = 2n^2\mathrm{Re}\left\{\Sigma_{0,\ell',\ell}(d_{m,n,\ell}\mathbf{b}_\ell)^H(d_{m,n,\ell'}\mathbf{b}_{\ell'})\right\}. \tag{69}$$

Combining (68) and (69), we obtain

$$\begin{aligned}\frac{\partial^2 f_{2,m,n}}{\partial\boldsymbol{\omega}\partial\boldsymbol{\omega}^T} &= 2n^2\mathrm{Re}\left\{\left(\mathbf{D}_{m,n}^H\mathbf{B}^H\mathbf{B}\mathbf{D}_{m,n}\right)\odot\boldsymbol{\Sigma}_0^T\right\} \\ &- 2n^2\mathrm{Re}\left\{\mathrm{Diag}\left(\mathbf{D}_{m,n}^H\mathbf{B}^H\mathbf{B}\mathbf{D}_{m,n}\boldsymbol{\Sigma}_0\right)\right\}.\end{aligned} \tag{70}$$

By noting that $f = -\sum_{m=1}^{M}\sum_{n=1}^{N}\beta(f_{1,m,n} + f_{2,m,n}) +$ const. and combining (60), (64), (67) and (70), we arrive at (44) and (45).

ACKNOWLEDGMENT

The authors would like to thank Chenshu Wu for his discussions and comments on the conference version of this work.

REFERENCES

[1] K. Xu, H. H. Chen, and C. Wu, "Pulse shape-aided multipath delay estimation for fine-grained WiFi sensing," in *Proc. IEEE 24th Int. Workshop Signal Process. Adv. Wireless Commun. (SPAWC)*, Sep. 2023, pp. 181–185.

[2] Y. Ma, G. Zhou, and S. Wang, "WiFi sensing with channel state information: A survey," *ACM Comput. Surveys (CSUR)*, vol. 52, no. 3, pp. 1–36, Jun. 2019.

[3] S. Tan, Y. Ren, J. Yang, and Y. Chen, "Commodity WiFi sensing in ten years: Status, challenges, and opportunities," *IEEE Internet Things J.*, vol. 9, no. 18, pp. 17832–17843, Sep. 2022.

[4] Y. He, Y. Chen, Y. Hu, and B. Zeng, "WiFi vision: Sensing, recognition, and detection with commodity MIMO-OFDM WiFi," *IEEE Internet Things J.*, vol. 7, no. 9, pp. 8296–8317, Sep. 2020.

[5] M. Kotaru, K. Joshi, D. Bharadia, and S. Katti, "SpotFi: Decimeter level localization using WiFi," in *Proc. ACM Conf. Special Interest Group Data Commun.*, Aug. 2015, pp. 269–282.

[6] K. Qian, C. Wu, Y. Zhang, G. Zhang, Z. Yang, and Y. Liu, "Widar2.0: Passive human tracking with a single Wi-Fi link," in *Proc. 16th Annu. Int. Conf. Mobile Syst., Appl., Services*, 2018, pp. 350–361.

[7] H. Abdelnasser, M. Youssef, and K. A. Harras, "WiGest: A ubiquitous WiFi-based gesture recognition system," in *Proc. IEEE Conf. Comput. Commun.*, Jun. 2015, pp. 1472–1480.

[8] Y. Zheng et al., "Zero-effort cross-domain gesture recognition with Wi-Fi," in *Proc. 17th Annu. Int. Conf. Mobile Syst. Appl. Services*, 2019, pp. 313–325.

[9] Y. Zeng, D. Wu, R. Gao, T. Gu, and D. Zhang, "FullBreathe: Full human respiration detection exploiting complementarity of CSI phase and amplitude of WiFi signals," *Proc. ACM Interact., Mobile, Wearable Ubiquitous Technol.*, vol. 2, no. 3, pp. 1–19, 2018.

[10] Y. Zeng, D. Wu, J. Xiong, E. Yi, R. Gao, and D. Zhang, "FarSense: Pushing the range limit of WiFi-based respiration sensing with CSI ratio of two antennas," *Proc. ACM Interact., Mobile, Wearable Ubiquitous Technol.*, vol. 3, no. 3, pp. 1–26, Sep. 2019.

[11] E. Perahia and R. Stacey, *Next Generation Wireless LANs: 802.11 n and 802.11 ac*. Cambridge, U.K.: Cambridge Univ. Press, 2013.

[12] D. Halperin, W. Hu, A. Sheth, and D. Wetherall, "Tool release: Gathering 802.11n traces with channel state information," *ACM SIGCOMM Comput. Commun. Rev.*, vol. 41, no. 1, p. 53, 2011, doi: 10.1145/1925861.1925870.

[13] Y. Xie, Z. Li, and M. Li, "Precise power delay profiling with commodity WiFi," in *Proc. 21st Annu. Int. Conf. Mobile Comput. Netw.*, 2015, pp. 53–64.

[14] F. Gringoli, M. Schulz, J. Link, and M. Hollick, "Free your CSI: A channel state information extraction platform for modern Wi-Fi chipsets," in *Proc. 13th Int. Workshop Wireless Netw. Testbeds, Exp. Eval. Characterization*, Oct. 2019, pp. 21–28.

[15] G. Taubock, F. Hlawatsch, D. Eiwen, and H. Rauhut, "Compressive estimation of doubly selective channels in multicarrier systems: Leakage effects and sparsity-enhancing processing," *IEEE J. Sel. Topics Signal Process.*, vol. 4, no. 2, pp. 255–271, Apr. 2010.

[16] S. Beygi, U. Mitra, and E. G. Ström, "Nested sparse approximation: Structured estimation of V2V channels using geometry-based stochastic channel model," *IEEE Trans. Signal Process.*, vol. 63, no. 18, pp. 4940–4955, Sep. 2015.

[17] S. Beygi, A. Elnakeeb, S. Choudhary, and U. Mitra, "Bilinear matrix factorization methods for time-varying narrowband channel estimation: Exploiting sparsity and rank," *IEEE Trans. Signal Process.*, vol. 66, no. 22, pp. 6062–6075, Nov. 2018.

[18] A. Elnakeeb and U. Mitra, "Bilinear channel estimation for MIMO OFDM: Lower bounds and training sequence optimization," *IEEE Trans. Signal Process.*, vol. 69, pp. 1317–1331, 2021.

[19] X. Zhang, L. Chen, M. Feng, and T. Jiang, "Toward reliable non-line-of-sight localization using multipath reflections," *Proc. ACM Interact., Mobile, Wearable Ubiquitous Technol.*, vol. 6, no. 1, pp. 1–25, 2022.

[20] E. Soltanaghaei, A. Kalyanaraman, and K. Whitehouse, "Multipath triangulation: Decimeter-level WiFi localization and orientation with a single unaided receiver," in *Proc. 16th Annu. Int. Conf. Mobile Syst., Appl., Services*, 2018, pp. 376–388.

[21] Z. Li, A. Nimr, P. Schulz, and G. Fettweis, "Superresolution wireless multipath channel path delay estimation for CIR-based localization," in *Proc. IEEE Wireless Commun. Netw. Conf. (WCNC)*, Apr. 2022, pp. 1940–1945.

[22] Z. Li, A. Nimr, P. Schulz, and G. Fettweis, "Multi-band superresolution multipath channel path delay estimation for CIR-based localization," in *Proc. 2nd IEEE Int. Symp. Joint Commun. Sens.*, Mar. 2022, pp. 1–6.

[23] Z. Li, A. Nimr, P. Schulz, and G. Fettweis, "A comparative study of subspace-based superresolution path delay estimation techniques," in *Proc. 26th Int. ITG Workshop Smart Antennas 13th Conf. Syst., Commun., Coding*, Feb. 2023, pp. 1–6.

[24] J. Li and U. Mitra, "Improved atomic norm based time-varying multipath channel estimation," *IEEE Trans. Commun.*, vol. 69, no. 9, pp. 6225–6235, Sep. 2021.

[25] A. Scaglione and X. Li, "Compressed channel sensing: Is the restricted isometry property the right metric?" in *Proc. 17th Int. Conf. Digit. Signal Process. (DSP)*, Jul. 2011, pp. 1–8.

[26] F. Gómez-Cuba and A. J. Goldsmith, "Compressed sensing channel estimation for OFDM with non-Gaussian multipath gains," *IEEE Trans. Wireless Commun.*, vol. 19, no. 1, pp. 47–61, Jan. 2020.

[27] K. Venugopal, A. Alkhateeb, N. G. Prelcic, and R. W. Heath, "Channel estimation for hybrid architecture-based wideband millimeter wave systems," *IEEE J. Sel. Areas Commun.*, vol. 35, no. 9, pp. 1996–2009, Sep. 2017.

[28] J. Rodríguez-Fernández, N. González-Prelcic, K. Venugopal, and R. W. Heath, "Frequency-domain compressive channel estimation for frequency-selective hybrid millimeter wave MIMO systems," *IEEE Trans. Wireless Commun.*, vol. 17, no. 5, pp. 2946–2960, May 2018.

[29] H.-R. Park and J. Li, "A frequency-domain SPICE approach to high-resolution time delay estimation," *IEEE Wireless Commun. Lett.*, vol. 7, no. 3, pp. 360–363, Jun. 2018.

[30] H. Park and J. Li, "High-resolution time delay estimation via sparse parameter estimation methods," *IET Signal Process.*, vol. 14, no. 2, pp. 97–105, Apr. 2020.

[31] F. Fereidoony, A. Jishi, M. Hedayati, Y. E. Wang, and S. Kowdley, "Magnitude–Delay least mean squares equalization for accurate estimation of time of arrival," *IEEE Sensors J.*, vol. 21, no. 16, pp. 18075–18084, Aug. 2021.

[32] T. Kazaz, G. J. M. Janssen, J. Romme, and A.-J. van der Veen, "Delay estimation for ranging and localization using multiband channel state information," *IEEE Trans. Wireless Commun.*, vol. 21, no. 4, pp. 2591–2607, Apr. 2022.

[33] M. Wu and C. Hao, "Super-resolution TOA and AOA estimation for OFDM radar systems based on compressed sensing," *IEEE Trans. Aerosp. Electron. Syst.*, vol. 58, no. 6, pp. 5730–5740, Dec. 2022.

[34] F. Bellili, S. B. Amor, S. Affes, and A. Ghrayeb, "Maximum likelihood joint angle and delay estimation from multipath and multicarrier transmissions with application to indoor localization over IEEE 802.11ac radio," *IEEE Trans. Mobile Comput.*, vol. 18, no. 5, pp. 1116–1132, May 2019.

[35] W. Gong and J. Liu, "RoArray: Towards more robust indoor localization using sparse recovery with commodity WiFi," *IEEE Trans. Mobile Comput.*, vol. 18, no. 6, pp. 1380–1392, Jun. 2019.

[36] B. H. Fleury, M. Tschudin, R. Heddergott, D. Dahlhaus, and K. I. Pedersen, "Channel parameter estimation in mobile radio environments using the SAGE algorithm," *IEEE J. Sel. Areas Commun.*, vol. 17, no. 3, pp. 434–450, Mar. 1999.

[37] D. Shutin and B. H. Fleury, "Sparse variational Bayesian SAGE algorithm with application to the estimation of multipath wireless channels," *IEEE Trans. Signal Process.*, vol. 59, no. 8, pp. 3609–3623, Aug. 2011.

[38] J.-J. Van De Beek, O. Edfors, M. Sandell, S. K. Wilson, and P. O. Borjesson, "On channel estimation in OFDM systems," in *Proc. IEEE 45th Veh. Technol. Conf.*, Jun. 1995, pp. 815–819.

[39] D. Vasisht, S. Kumar, and D. Katabi, "Decimeter-level localization with a single WiFi access point," in *Proc. 13th USENIX Symp. Netw. Syst. Design Implement. (NSDI)*, 2016, pp. 165–178.

[40] D. G. Tzikas, A. C. Likas, and N. P. Galatsanos, "The variational approximation for Bayesian inference," *IEEE Signal Process. Mag.*, vol. 25, no. 6, pp. 131–146, Nov. 2008.

[41] T. M. Cover, *Elements of Information Theory*. Hoboken, NJ, USA: Wiley, 1999.

[42] C. M. Bishop and N. M. Nasrabadi, *Pattern Recognition and Machine Learning*, vol. 4. Cham, Switzerland: Springer, 2006.

[43] M. E. Tipping, "Sparse Bayesian learning and the relevance vector machine," *J. Mach. Learn. Res.*, vol. 1, pp. 211–244, Sep. 2001.

[44] D. P. Wipf and B. D. Rao, "Sparse Bayesian learning for basis selection," *IEEE Trans. Signal Process.*, vol. 52, no. 8, pp. 2153–2164, Aug. 2004.

[45] S. Ji, Y. Xue, and L. Carin, "Bayesian compressive sensing," *IEEE Trans. Signal Process.*, vol. 56, no. 6, pp. 2346–2356, Jun. 2008.

[46] X. Tan and J. Li, "Computationally efficient sparse Bayesian learning via belief propagation," *IEEE Trans. Signal Process.*, vol. 58, no. 4, pp. 2010–2021, Apr. 2010.

[47] X. Zou, F. Li, J. Fang, and H. Li, "Computationally efficient sparse Bayesian learning via generalized approximate message passing," in *Proc. IEEE Int. Conf. Ubiquitous Wireless Broadband (ICUWB)*, Oct. 2016, pp. 1–4.

[48] H. Duan, L. Yang, J. Fang, and H. Li, "Fast inverse-free sparse Bayesian learning via relaxed evidence lower bound maximization," *IEEE Signal Process. Lett.*, vol. 24, no. 6, pp. 774–778, Jun. 2017.

[49] A. Lin, A. H. Song, B. Bilgic, and D. Ba, "Covariance-free sparse Bayesian learning," *IEEE Trans. Signal Process.*, vol. 70, pp. 3818–3831, 2022.

[50] M. R. Hestenes and E. Stiefel, "Methods of conjugate gradients for solving linear systems," *J. Res. Nat. Bureau Standards*, vol. 49, no. 6, pp. 409–436, Dec. 1952.

[51] L. Hu, Z. Shi, J. Zhou, and Q. Fu, "Compressed sensing of complex sinusoids: An approach based on dictionary refinement," *IEEE Trans. Signal Process.*, vol. 60, no. 7, pp. 3809–3822, Jul. 2012.

[52] E. Leitinger, S. Grebien, B. Fleury, and K. Witrisal, "Detection and estimation of a spectral line in MIMO systems," in *Proc. Asilomar Conf. Signals, Syst. Comput.*, Nov. 2020, pp. 1090–1095.

[53] S. Grebien, E. Leitinger, K. Witrisal, and B. H. Fleury, "Super-resolution estimation of UWB channels including the dense component—An SBL-inspired approach," *IEEE Trans. Wireless Commun.*, early access, Feb. 29, 2024, doi: 10.1109/TWC.2024.3371352.

[54] K. Witrisal, E. Leitinger, S. Hinteregger, and P. Meissner, "Bandwidth scaling and diversity gain for ranging and positioning in dense multipath channels," *IEEE Wireless Commun. Lett.*, vol. 5, no. 4, pp. 396–399, Aug. 2016.

[55] T. Wilding, S. Grebien, U. Mühlmann, and K. Witrisal, "AoA and ToA accuracy for antenna arrays in dense multipath channels," in *Proc. 8th Int. Conf. Localization GNSS (ICL-GNSS)*, Jun. 2018, pp. 1–6.

[56] J. Kulmer, S. Grebien, E. Leitinger, and K. Witrisal, "Delay estimation in presence of dense multipath," *IEEE Wireless Commun. Lett.*, vol. 8, no. 5, pp. 1481–1484, Oct. 2019.

[57] H. L. Van Trees, *Detection, Estimation, and Modulation Theory, Part I: Detection, Estimation, and Linear Modulation Theory*. Hoboken, NJ, USA: Wiley, 2004.

[58] P. G. Stoica and R. L. Moses, *Introduction to Spectral Analysis*. Upper Saddle River, NJ, USA: Prentice-Hall, 1997.

[59] R. Du et al., "An overview on IEEE 802.11bf: WLAN sensing," 2023, *arXiv:2310.17661*.

[60] Y. Xie, J. Xiong, M. Li, and K. Jamieson, "Md-track: Leveraging multi-dimensionality for passive indoor Wi-Fi tracking," in *Proc. 25th Annu. Int. Conf. Mobile Comput. Netw.*, Aug. 2019, pp. 1–16.

[61] A. Goldsmith, *Wireless Communications*. Cambridge, U.K.: Cambridge Univ. Press, 2005.

[62] W. Li, W. Yao, and P. J. Duffett-Smith, "Improving the sage algorithm with adaptive partial interference cancellation," in *Proc. IEEE 13th Digit. Signal Process. Workshop 5th IEEE Signal Process. Educ. Workshop*, Jan. 2009, pp. 404–409.

[63] P. J. Chung and J. F. Böhme, "DOA estimation using fast EM and SAGE algorithms," *Signal Process.*, vol. 82, no. 11, pp. 1753–1762, Nov. 2002.

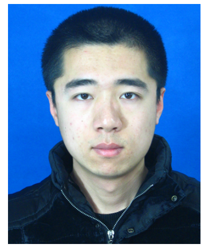

Ke Xu received the B.E. and M.E. degrees from the University of Electronic Science and Technology of China in 2017 and 2020, respectively. He is currently pursuing the Ph.D. degree with The Chinese University of Hong Kong. His research interests include wireless sensing.

Rui Zhang received the Ph.D. degree from The University of Sydney in December 2020. He is currently with the Department of Information Engineering, The Chinese University of Hong Kong. His research interests include machine learning in wireless communications and wireless sensing and localization systems.

He (Henry) Chen (Member, IEEE) received the Ph.D. degree in electrical engineering from The University of Sydney, Australia, in 2015. Following his graduation, he was a Research Fellow with the School of Electrical and Information Engineering, The University of Sydney. In 2019, he accepted a faculty position with the Department of Information Engineering, The Chinese University of Hong Kong, where he is currently an Assistant Professor. His research interests include wireless communications and networking, wireless sensing, and their applications in robotics. From 2020 to 2022, he was a member of the Editorial Board of the IEEE WIRELESS COMMUNICATIONS LETTERS. He also serves on the Editorial Board for IEEE TRANSACTIONS ON WIRELESS COMMUNICATIONS.